

# Fine-scale Altimetry and the Future SWOT Mission

Rosemary Morrow<sup>1</sup>, Denis Blumstein<sup>1,2</sup>, and Gerald Dibarboure<sup>2</sup>

<sup>1</sup>LEGOS/CNRS/IRD/CNES/University Toulouse III, Toulouse, France; <sup>2</sup>CNES, Toulouse, France

*This chapter describes recent advances in improving altimetry observations over the ocean for the detection of fine-scale ocean dynamics. The first section gives an overview of the different satellite radar altimetry techniques being used today at high-resolution over the open and coastal oceans: from conventional along-track nadir altimetry to along-track Synthetic Aperture Radar (SAR) at nadir. We present the advantages of the measurement techniques in conventional Ku-band (Jason) and Ka-band (Saral), and in global SAR mode (Sentinel-3). We show how the along-track errors are estimated, how they vary geographically and seasonally, and how they limit the sea surface height (SSH) scales resolved. We also address various mapping techniques being used to derive gridded SSH data and the issues for observing fine-scale ocean dynamics from altimeter data in the coastal zone. The second section addresses the future global SAR-interferometry mission, Surface Water Ocean Topography (SWOT), which aims to measure terrestrial surface waters and ocean SSH over a wide swath. We concentrate on the ocean component of this mission, which will provide the first two-dimensional (2D) observations of SSH on a 1-2 km grid. The low noise level of the SWOT observations should allow us to observe physical processes in the open and coastal oceans with wavelength scales down to 15-20 km. We present the SWOT SAR-interferometry technique, as well as the mission's sampling characteristics and error budget. Of particular interest is the range of ocean dynamics that have a SSH signature in the wavelength scale of 15-200 km, including small mesoscale structures, larger submesoscale fronts and filaments, internal tides, and internal gravity waves. These are difficult to observe with the present altimeter constellation due to the along-track altimetric sampling and higher noise levels. The chapter addresses how these fine-scale dynamics will be observed with the future SWOT SAR-interferometric altimetry technology, the challenges in mapping the SWOT swath SSH observations, and the preparation to assimilate SWOT 2D SSH images into operational ocean models.*

## Fine-scale Ocean Dynamics from Conventional and SAR Altimetry

### Introduction

Spaceborne altimetry measurements were first demonstrated in the 1970s (Skylab, GEOS-3, Seasat) with a sea surface height (SSH) accuracy of around 1 m, mainly due to orbit determination errors. In the late 1980s, the Geosat mission (US Navy, 1985-1990) demonstrated the ability to monitor the ocean from space, with an 18-month geodetic phase to improve the Earth's gravity and marine geoid estimates, followed by a three-year ocean circulation phase. The era of high-precision satellite altimetry started with the launch of Topex/Poseidon in 1992, a joint NASA–CNES mission that provided the first estimates of SSH with 2–3 cm accuracy

Morrow, R., D. Blumstein, and G. Dibarboure 2018: Fine-scale altimetry and the future SWOT mission. In "New Frontiers in Operational Oceanography", E. Chassignet, A. Pascual, J. Tintoré, and J. Verron, Eds., GODAE OceanView, 191-226, doi:10.17125/gov2018.ch08.

on a 10-day repeat cycle. Since then, several high-precision altimetry missions have been launched: Jason-1, Jason-2, Jason-3, as successors to Topex/Poseidon. Complementary space–time coverage over all surfaces was available from ERS-1&2 and Envisat (missions from ESA), SARAL/AltiKa (joint mission from CNES and ISRO), and HY-2 (CNES and CSA-China). All of these missions are in conventional “low-resolution” mode (LRM).

A new generation of altimeters is starting to use nadir Synthetic Aperture Radar (SAR) and SAR interferometry modes, including CryoSat-2 (ESA) and the first global SAR altimetry mission from Sentinel-3A (ESA). In the future, global SAR nadir missions will continue with Sentinel-3B (ESA) and the reference climate mission, Jason-CS/Sentinel 6A (ESA, EUMETSAT, NOAA, CNES, and NASA), part of the operational Copernicus program of the European Union.

In this first section, we detail some of the characteristics and advances of the most recent LRM missions in Ku- and Ka-band, as well as their differences from the SAR along-track missions. In the second section, we present the wide-swath SAR interferometric altimetry mission (Surface Water Ocean Topography or SWOT) able to study the two-dimensional (2D) fine-scale ocean circulation and terrestrial surface waters, jointly developed by NASA and CNES. The different radar altimeter missions providing data from 1992 onwards are shown in Table 8.1, after Frappart et al. (2017).

Mission	Topex/Poseidon Jason-1/2/3	ERS-2 ENVISAT	CryoSat-2	SARAL	Sentinel-3 A, B	Jason-CS/ Sentinel-6	SWOT
Instrument	NRA/SSALT Poseidon-2 Poseidon-3 Poseidon-3B	RA RA-2	SIRAL	AltiKa	SRAL	Poseidon-4	KaRIN Poseidon-3 like
Space agency	CNES, NASA	ESA	ESA	CNES, ISRO	ESA	ESA, EUMETSAT, NOAA, CNES	CNES, NASA
Operation	1992-2005 2001-2013 Since 2008 Since 2016	1995-2003 2002-2012	Since 2010	Since 2013	Since 2016 Expected in 2017	Expected in 2020	Expected in 2021
Acquisition mode	LRM	LRM	LRM, SAR, InSAR	LRM	LRM, SAR	LRM, SAR	InSAR LRM
Acquisition	Along-track	Along-track	Along-track	Along-track	Along-track	Along-track	120 km swath Along-track
Frequency (GHz)	13.575 (Ku) 5.3 (C)	13.8 (Ku) <sup>b</sup> 13.575 (Ku) <sup>c</sup> 3.2 (S) <sup>e</sup>	13.575 (Ku)	35.75 (Ka)	13.575 (Ku) 5.41 (C)	13.575 (Ku) 5.3 (C)	35.6 (Ka) 13.575 (Ku) 5.3 (C)
Altitude (km)	1315	800	717	800	814.5	1315	890
Orbit inclination (°)	66	98.55	92	98.55	98.65	66	77.6
Repetitivity <sup>a</sup> (days)	9.9156	35	369	35	27	9.9156	21
Equatorial cross-track separation* (km)	315	75	7.5	75	104	315	133.1

<sup>a</sup> On nominal orbit

<sup>b</sup> RA onboard ERS-2

<sup>c</sup> RA-2 onboard ENVISAT

**Table 8.1.** Major characteristics of the high-precision radar altimetry missions since 1992

## Conventional low-resolution mode (LRM) altimetry; examples from the Jason series and Saral

The satellite radar altimetry measurement technique is based on an active radar emission at microwave frequencies from the satellite platform. A detailed description can be found in Chelton

et al. (2001) and others (e.g., Robinson, 2004; Frappart et al., 2017; Escudier et al., 2017). We provide here a simplified view that allows a user to understand how the measurement is formed.

The radar sensor emits an electromagnetic pulse in the nadir direction (vertically downwards) and precisely measures the two-way travel time of the signal ( $\Delta t$ ) between the satellite and the reflecting surface. Given the known speed of light in a vacuum,  $c$ , the distance or range,  $R$ , between the sensor the reflecting surface, such as the ocean, can be given by:

$$R = \frac{c\Delta t}{2} - \sum_i \Delta R_i \quad (1)$$

where  $\Delta R_i$  represent the sum of the corrections in the delay of the round trip travel time, due to atmospheric, instrument, or surface effects.

In reality, to obtain a height resolution of around 1 cm, we would need a pulse of a fraction of a nanosecond (with a pulse bandwidth of  $> 3$  GHz, which is not possible). So altimetry uses a technique called pulse compression. The emitted signal has a frequency that is linearly modulated in time (a chirp). When the return signal (echo) is received onboard, the radar passes the signal through an inverse filter to compress the chirp back into a short pulse and recover the required range resolution (for details see Chelton et al., 2001).

Over an ocean surface, the altimeter sends out the radar energy, which is reflected back from the sea surface. Even if the emitted signal has an infinitely short duration, the return echo has a longer duration because it is scattered back by many reflectors on the surface that are at different distances from the radar (see Figure 8.1). The power of the return signal has a resolution of many tens of centimeters (about 47 cm for altimeters of the Jason series), which is not sufficient to study cm-level ocean SSH signals. However, if we apply a theoretical model, we can analyze how the power is returned from a series of gates/bins, each at a slightly different time (see Figure 8.1). This return power over time is called a “waveform” and it has a characteristic shape that can be described analytically (for example, over the open ocean by the Brown [1977] model) or numerically. The waveform shape and amplitude provide information on the nature of the surface and the geophysical parameters we wish to derive (SSH, significant wave height, wind speed, antenna mispointing). In the Brown model, the altimeter range ( $R$ ) corresponds to the time ( $\tau$  or epoch at mid-height) when the received power reaches the middle of the leading edge (see Figure 8.1). Using the epoch given by the Brown model allows us to obtain the centimeter precision from the original signal with a sampling step of 47 cm (2%). In addition, the power of the return signal gives information on the backscattering coefficient, from which the wind speed (amplitude, not direction) can be derived using empirical algorithms. The significant wave height is derived from the slope of the waveform’s leading edge, and the antenna mispointing from the trailing edge slope.

The Brown model’s validity is limited to conditions where the characteristics of the water surface and the transmission through the atmosphere are very uniform. In the open ocean, this is generally true but, in some cases, the validity conditions are not met and the accuracy of the Brown model’s range retrievals deteriorates. This occurs, for example, when the ocean backscatter or surface roughness varies rapidly (e.g., across low wind patches or near the coast when the ocean signal is polluted by the nearby land) or in cases of heavy rain cells. The occurrence of such events can be monitored and edited using the backscatter coefficient (e.g., Quartly et al., 2001; Dibarboure

et al., 2014). Conventional radar altimeters provide measurements at a frequency around 10 Hz (T/P, ERS), 20 Hz (Jason, Envisat, CryoSat2), and 40 Hz (AltiKa). Each of these measurements is the (incoherent) sum of about 100 individual echos, and the summing helps reduce the measurement noise.

Figure 8.1 also shows a schematic of the pulses’ “round” footprint on the ocean surface. For the Jason class altimeters, flying at 1336 km altitude, and for the pulses averaged over 1 second, this footprint is more oval in shape, being around 10 km along-track and 5 km cross-track (Chelton et al., 2001). The SSH signal and any noise effects are integrated over the original footprint domain (50-70 km<sup>2</sup>), and then averaged over the 1-second time. The footprint size is determined by the pulse duration (3 ns <-> 2 km for calm seas) but also depends on the sea state conditions, the altimeter frequency band, the antenna pattern and the satellite altitude. As an example, for a 3 m high significant wave height sea, the footprint cross-track radius is around:

- 3 km for Ka-band Saral at ~800 km altitude;
- 4.4 km for Ku-band Envisat at ~800 km altitude
- 5.5 km for Ku-band Jason at 1336 km altitude.

The footprint size also increases in high seas as the sea-state increases. For example, 10 m high significant wave height increases the footprint for Envisat to 7.7 km, and to 9.6 km for Jason (Chelton et al., 1989).

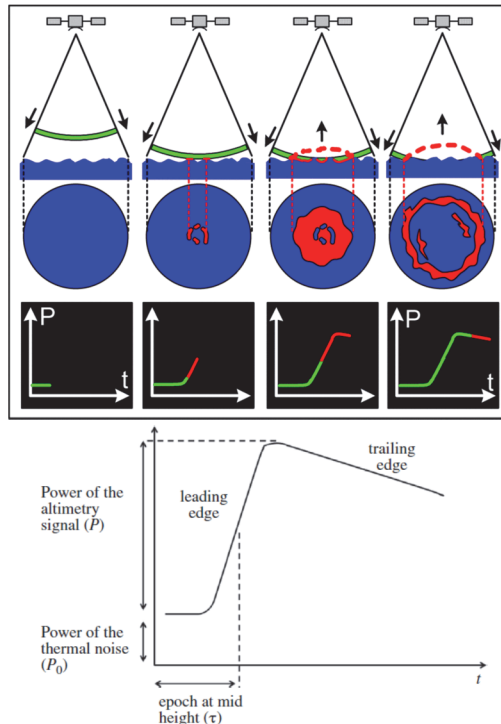


**Figure 8.1.** Schematic of a time series of a radar pulse. In green, the outgoing radar pulse before it reaches the surface, in red, the pulse reflected from an ocean surface with waves received back at the sensor. The bottom panels show the radar power received at the sensor over time. The main waveform parameters marked are derived from the Brown model, used to determine the different altimetric geophysical parameters. (Credits: CNES)

To obtain a precise estimate of the sea surface topography, the range has to be adjusted for instrument corrections, atmospheric propagation delays (as the radar pulse passes through the wet and dry atmosphere, or due to interactions with the electron content in the ionosphere), and surface geophysical corrections. The details of this processing can be found in Chelton et al. (2001), Pujol et al. (2016), and Escudier et al. (2017). Surface geophysical corrections need to be applied to remove the effects of tides (ocean tides, solid earth tides, loading tides, and the pole tide), rapid atmospheric dynamical effects from wind and pressure forcing that are not resolved by the altimeter temporal sampling, and corrections for the geoid or mean sea surfaces.

The Saral/AltiKa altimeter is the first altimeter to use a high single frequency in Ka-band (35.75 GHz). Ka-band is much less attenuated by the ionosphere than the Ku-band, and is designed to have greater performance in terms of vertical resolution, time decorrelation of echoes, spatial resolution and range noise (Verron et al., 2015). Theoretically, Ka-band pulses are sensitive to rain; however, Saral does not exhibit large missing data during rain events, except for strong rain rates. The Ka-band wavelength is better suited to describing the slopes of small facets on the sea surface (capillary waves, etc.) and gives a more accurate measurement of the backscatter coefficient over calm or moderate seas. Saral also has a smaller footprint and higher resolutions (40 Hz as opposed to 20 Hz for other altimeters), leading to a noise reduction of a factor of two compared to Jason-class altimeters for wave heights greater than 1 m. The increased spatial resolution and lower noise are associated with a more focused cross-track footprint for Saral, being nearly half the size of the Jason-class altimeters.

---

### Along-track SAR altimetry, Cryosat-2, Sentinel-3

We have seen that the LRM altimetry is based on the pulse compression of a series of individual radar pulses and, when averaged over 1000s of pulses (at 1Hz), the footprint size is expanded beyond the normal pulse-limited diameter. The main interest of the SAR processing is to provide a greatly reduced footprint (less than 5 km<sup>2</sup> for SARM) compared to conventional LRM measurements, which have a footprint size of more than 200 km<sup>2</sup>. This gain in spatial resolution is in the direction of displacement of the satellite (along-track). Delayed Doppler/SAR altimetry exploits a coherent processing of groups of transmitted pulses in order to zoom in on a smaller along-track bin (Raney, 1998; Boy et al., 2017; Frappart et al., 2017; Escudier et al., 2017). Although the SAR processing is complex, the basic principle is based on the Doppler effect due to the moving satellite.

Consider the frequency shift caused by the Doppler effect generated by the moving satellite, which affects the signal coming from a given scattering point within the footprint on the ground. If the satellite flies horizontally, the Doppler shift is zero for the scattering point at nadir, but it increases almost linearly with the along-track distance between the scatterer and the nadir point. Figure 8.2d shows a schematic of this effect. The straight lines correspond to contours of equal linear Doppler shift and the circles are a selection of contours of equal range seen from the radar. The satellite is moving to the right along the track in this schematic. In essence, the SAR processing identifies the exact position of the return power and removes the power coming from all the vertical

bands shown on Figure 8.2 except from the central band (called the zero Doppler band), whose width is typically 340 m. This is then repeated for the adjacent Doppler bands to form a stack of waveforms. This is analogous to the pulse compression technique used for range compression. For the pulse compression in range (cross-track or perpendicular to the flight direction), the linear variation of frequency in time is imposed by the instrument, whereas it is imposed by the Doppler frequency shift for the pulse compression in azimuth (along-track).

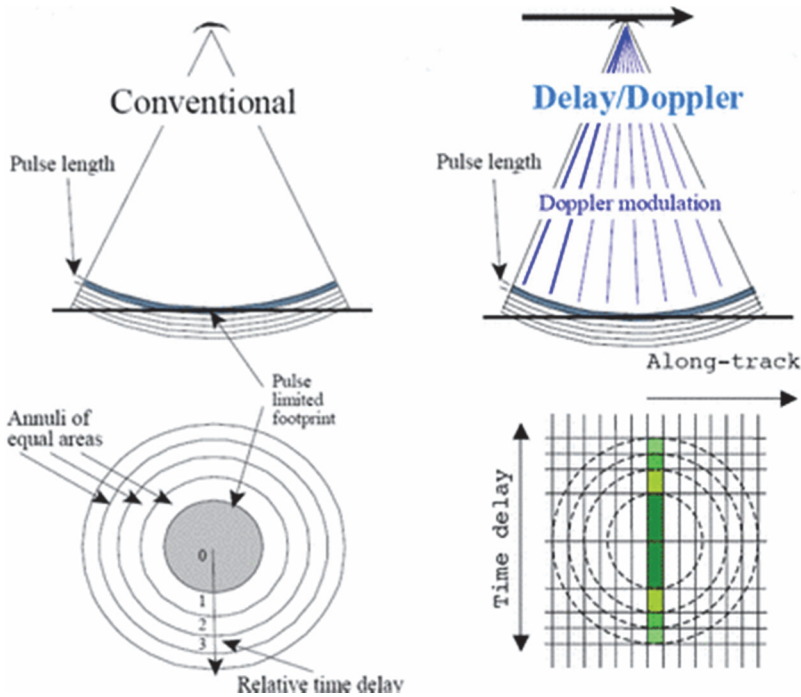


**Figure 8.2.** (left panels): Schematic of conventional LRM pulse-limited altimetry showing the concentric annuli of pulses being reflected back to the satellite, and contributing to the steady increase in power over the Brown waveform. (right panels): SAR uses a combination of the range information and the time delay. Here the circles represent the iso-range contours and vertical lines the isodoppler contours). The horizontal line is the trajectory of the satellite. (Credits: R.K. Raney, Johns Hopkins University Applied Physics Laboratory)

As the satellite moves along-track, the same vertical band in Figure 8.2d can be observed many times from the front of the round footprint, then the centre, then the back. A multi-looking technique is used in the SAR processing, taking the sum of the contribution of many co-located vertical bands during a 2 sec period, instead of just analyzing the millisecond observation from individual pulses. The advantage of this “stacking” within the SAR processing is that the averaged return signal (and integrated noise) are concentrated in the smaller central zero Doppler band, being 340 m along-track and ~5 km across track. In comparison, the convention LRM mode has the signal and noise integrated over the spherical diameter surface (Figure 8.2), whose footprint size varies depending on frequency, altitude, and surface roughness conditions. The SAR processing gives a more focused signal, and a much smaller noise level, since the noise is integrated over a smaller surface area with less sensitivity to sea-state. It can also approach closer to the coast or islands or sea-ice, with fewer perturbations to the radar signal when the ground track is perpendicular to the coast/sea-ice boundary.

---

## Improvements in along-track data and mapping capabilities

Over the last decade, there have been important advances in the processing and reprocessing of the along-track altimeter data from all missions, as well as in the quality of the multi-mission mapping by DUACS/AVISO, which is used in most oceanographic studies. Although the mesoscale band is the most energetic component of sea level, small-scale errors and noise are two of the factors limiting our observation of the smaller mesoscales. The choice of editing, filtering, or mapping can also impact on the ocean signals we can observe. Here, we give a brief overview of the recent improvements in along-track data processing and multi-mission mapping.

### **Reprocessing of along-track data**

Many studies use the along-track sea level anomaly (SLA) data directly (for example, for calculating along-track wavenumber spectra, for calculating fine-scale currents in a local area, or for assimilation in models). There have been many improvements in the quality of these along-track data, described in detail by Dibarboure et al. (2011) and aided by the ESA Climate Change Initiative effort (Ablain et al., 2015). The most recent altimeter datasets have been reprocessed using the latest standards for climate studies and applied homogeneously to all missions. The radar waveforms have been reprocessed, rigorous editing and selection processes have been applied, especially important in coastal and high-latitude regions, and the most up-to-date standards applied for orbits and atmospheric forcing (Ablain et al., 2015). This has improved the signal-to-noise for each mission.

The next step is to cross-calibrate the different altimeter missions within the constellation. This is done first between the reference missions (T/P, J1, J2, J3) to reduce the long wavelength, geographically correlated errors. A second cross-calibration is then performed to reduce the long wavelength errors between the reference missions and the other altimeter missions. The details are described in Dibarboure et al. (2011) and Pujol et al. (2016). The long wavelength reduction removes orbit errors, as well as errors in the tidal corrections, atmospheric forcing corrections, or in the mean sea surface for non-repeat altimeter missions. This can potentially improve the quality of the mapped mesoscale signals.

Once the missions are cross-calibrated, SLAs are calculated by removing a reference surface: either a precise time-mean along-track profile (for the missions on a long-term repeating track) or a gridded 2D mean sea surface product (for the new missions or non-repeating missions). There has been recent progress in improving the time-mean along-track profile calculation over a 20-year period, especially in coastal and high-latitude regions (Pujol et al., 2016), and a new generation of 2D mean sea surface products are being developed using more geodetic altimeter data from Cryosat-2 and Jason-1 (DTU2015; O. Anderson; CNES-CLS-2015; P. Schaeffer; pers. Communication). These improvements in the mean sea surface have a direct impact on the mesoscale SLAs, as shown by Pujol et al. (2016) and Dufau et al. (2016).

Finally, due to the limited temporal sampling of the altimeters, rapid barotropic signals are not well-resolved. In the mapped and along-track SLA data, their high-frequency component  $< 20$  days is removed using a dynamical atmospheric correction (DAC) based on a barotropic model forced by wind and atmospheric pressure (Carrère and Lyard, 2003). This is a relatively large-scale

correction and should not impact the barotropic component of the mesoscale dynamics, except in the coastal zone where the DAC correction has higher resolution and resolves smaller scales. In general, the corrected altimetric data represents both barotropic and baroclinic motions at mesoscales.

### Multi-mission mapping

Since 1992, the altimeter constellation has varied over time, having two to four altimeter missions available that can be combined for better spatial-temporal resolution of the mesoscale field (Table 1). Jason-class altimeters follow a repeat cycle of ten days designed to monitor ocean variations so they pass over the same points fairly frequently, but their ground tracks are some 315 km apart at the equator – more than the average span of an ocean eddy. On the other hand, ERS/Envisat and Saral only revisit the same point on the globe every 35 days, but the maximum distance between two tracks at the equator is just 80 kilometers. Figure 3.2.3 shows an example of the spatial coverage of the altimeter constellation in June 2015 in the Mediterranean Sea, with all tracks cumulated over one day and ten days. Combining these different sampling missions gives a much better spatial-temporal evolution of the ocean circulation. Even after ten days, some regions are well-sampled, but others still have gaps of ~150 km.

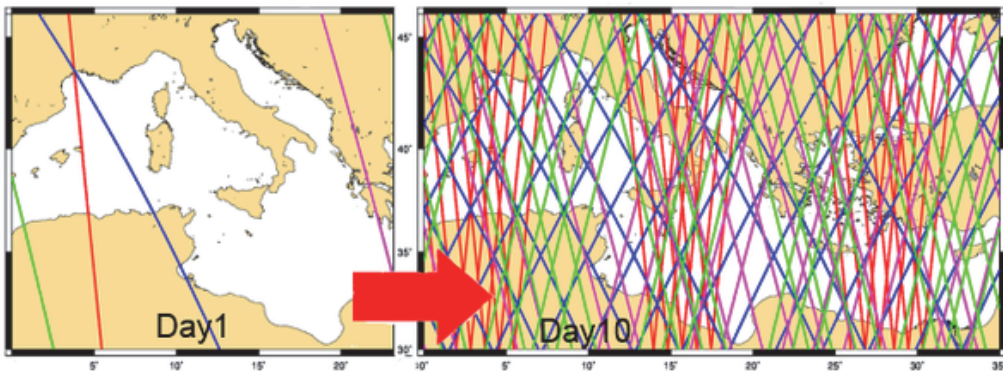


**Figure 8.3.** Grounds tracks for the four operational satellites on June 2015, over the Mediterranean Sea: Jason-2 ground tracks are blue, Saral/AltiKa are green, Cryosat-2 are red, and HY-2A are pink. (Credits: AVISO)

Multi-mission merged SLA maps are used for ocean studies, where the along-track data are sub-optimally interpolated onto a fixed grid using Gaussian spatial and temporal decorrelation functions (Dibarboure et al., 2011). Two series of maps exist. The first is a two-satellite or “reference” series of maps that has consistent sampling over the entire period from 1992 to 2015 using data from T/P-J1-J2 and ERS-Envisat-Saral (Cryosat-2 data is used in the small gap between Envisat and Saral). This allows consistent sampling for long-term studies of interannual variability. A second “all-satellite” series of maps includes data from all available missions, with increased spatio-temporal sampling. This is available from 2000 onwards, and provides better anisotropic structure for mesoscale studies (Pascual et al., 2006) and improved sea level and velocity variances, which are used to evaluate the realism of ocean circulation models (Le Traon and Dibarboure, 2002). An example of the mapping for the two series is given for the Mediterranean Sea for one date, in Figure 8.4.

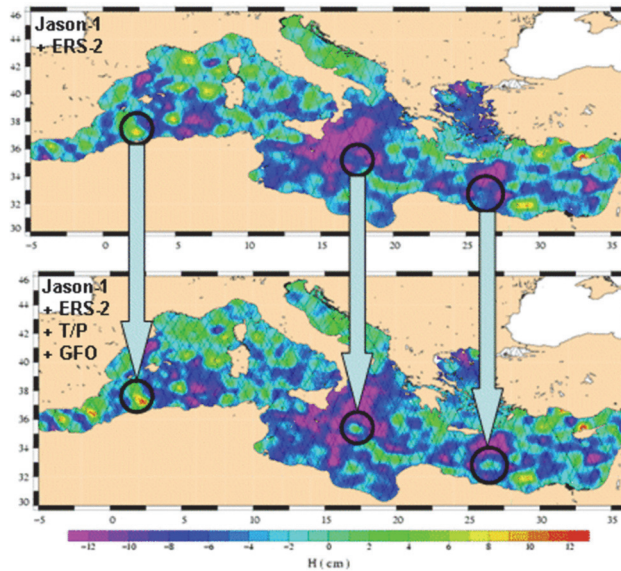


**Figure 8.4.** SLA maps over the Mediterranean on June 11, 2003, made from Jason-1 + ERS-2 (top) and Jason-1+ERS-2+T/P+GFO (bottom). Merging of the four satellite data shows eddies (circles) that are invisible or just barely visible with two satellites and much better sorted out with four of them. (Credits: A. Pascual, IMEDEA).

The latest version of the DUACS DT2014 gridded products are described in (<https://www.aviso.altimetry.fr/en/data/products/sea-surface-height-products/global.html>) and have a number of advantages for mesoscale applications (Pujol et al., 2016). The data are referenced to a 20-year period, which provides better interannual variability; the editing has been improved and homogeneous standards applied to all missions; the along-track data input in the system have less filtering, maintaining scales down to 65 km wavelength (older versions had along-track filtering to 250 km in the tropics, decreasing to higher latitudes); the gridded data are available daily on a  $1/4^\circ$  Cartesian grid, reducing interpolation errors for users converting from the original  $1/3^\circ$  Mercator grid; correlation scales vary regionally (correlation scale maps are given in Dibarboure et al., 2011); and the error budget varies regionally and between missions depending on data quality. These processing changes allow additional mesoscale signals at wavelengths less than 250 km, and the global SLA variance has increased by 5%; the EKE variance by 15%. This has particular benefits for mesoscale studies in the boundary region, as noted by Capet et al. (2014) for the eastern boundary upwelling systems.

The mean wavelength resolution of these gridded products remains  $2^\circ$ , i.e., 200 km at mid latitudes (Chelton et al., 2011). A comparison with the along-track data shows that in the 65-300 km mesoscale band, around 40% of the mesoscale variability is missing in these gridded products, mainly associated with the smaller mesoscale signals (this depends very much on latitude) (Pujol et al., 2016). A second consequence of the reduced along-track filtering is that additional signals are now observed, associated with residual internal tide signals in both the along-track and mapped products (Ray and Zaron, 2015; Dufau et al., 2016). As we resolve smaller-scale structures, the separation and identification of internal tides and internal waves becomes more critical. Despite the

progress in improving the along-track signal-to-noise, mesoscale studies today are still limited by this along-track noise and the altimeter ground track sampling.

The improved coverage in recent years has allowed a number of regional gridded products to be developed in the Mediterranean Sea (Pujol and Larnicol, 2005; Pascual et al., 2005), the Black Sea, the Mozambique region, the Arctic Ocean, and other regions (see <https://www.aviso.altimetry.fr/en/data/products/sea-surface-height-products/regional.html>).

Regional studies have created gridded altimeter products with correlation scales that are better tuned to the local dynamics, allowing smaller-scale processes in the coastal zone (Dussurget et al., 2011) or including anisotropic scales associated with bathymetry (Escudier et al., 2012). As an alternative to the statistical optimal interpolation, Ubelmann et al. (2015) recently developed a simple dynamical interpolation method to retrieve SSH in the temporal gap between two SSH fields separated by up to 20 days. This experimental method, based on the conservation of potential vorticity and assuming that most of the SSH variability is carried by the first baroclinic mode, was able to reconstruct gridded SSH maps with wavelengths smaller than 150 km. A more recent version uses the simple dynamical model to introduce dynamical time-evolving structure into covariance functions, which are then applied in an optimal interpolation framework using along-track altimeter data (Ubelmann et al., 2016). Simulations in the Gulf Stream region show reduced mapping errors and a better representation of the smaller-scale eddies.

---

## Global along-track wavenumber spectra of altimetry data: quantifying errors and observable scales

Altimeters fly at 7 km/s and cross ocean basins in a few minutes, providing a “snapshot” of the interaction of different spatial scales of ocean variability. Many altimeter missions on repeat tracks have these snapshots repeated every ten to 35 days, over decadal time periods. This global and decadal coverage from the series of repeating satellite altimetry missions with high along-track resolution provides a unique framework for estimating frequency-wavenumber spectra of ocean SSH variability. Figure 8.5 shows the globally-averaged wavenumber spectrum of SLA from different altimeter missions with different technology at fine resolution: Jason Ku-band LRM (20 Hz), Saral Ka-band LRM (40 Hz), and Sentinel-3 SAR (20 Hz). The wavenumber spectrum of SSH or SLA is generally ‘red,’ with the largest SSH fluctuations on the largest spatial scales and increasingly smaller fluctuations at smaller scales. This decrease of SSH signal with decreasing spatial scale means that the smallest spatial scales that can be resolved are limited by the noise floor of the altimeters.

Figure 8.5a shows that these three missions with different ground tracks are observing similar ocean SLA power spectral density at large scales and the same cascade of spectral energy down to scales of 100 km (wavenumber of  $10^{-2}$  cycles per km - cpkm). At smaller scales, from 100-10 km (wavenumber of  $10^{-2}$  to  $10^{-1}$  cpkm), the three missions observe very different SLA energy. Jason-2 (in green) has a large spectral “bump” from 10-30 km wavelength due to inhomogeneous sea-state perturbations within the altimeter footprint (wind, waves, rain cells, ...; Dibarboure et al., 2014). Since the Jason-2 altimeter footprint is relatively large, these conditions add more noise, masking

the ocean signal out to 70-100 km wavelength. Saral and Sentinel-3 SAR mode have smaller footprints and are designed to have lower noise. Saral still shows a spectral “bump” at smaller scales, mainly due to sea-state effects that mask the ocean signal out to scales of 30-50 km. Sentinel-3 SAR technology shows a different red noise slope at small wavelengths and a greatly reduced noise level compared to the Jason-class of altimeters. Work is ongoing to understand the spectral shape of SAR instrument noise in varying wind-wave-swell conditions and the impact of small-scale ocean signals such as internal waves on this red spectral slope.

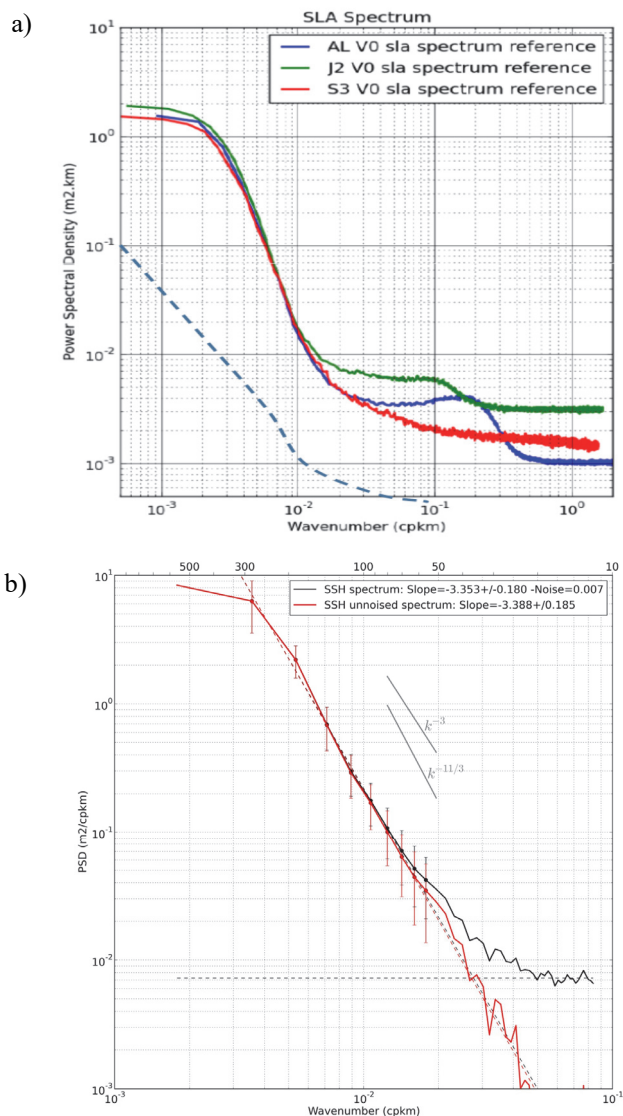


**Figure 8.5.** a) Global mean SLA wavenumber spectra from high-resolution along-track altimetry data from Jason-2-LRM (in green), Saral-LRM (in blue) and Sentinel-3 SAR (in red). 20 Hz data are used for Jason and Sentinel-3, Saral is at 40 Hz. The dashed line shows the projected SWOT error levels. b) An example of mean SSH wavenumber spectra from 1 Hz along-track Jason-2-LRM in a  $10 \times 10^\circ$  box in the Kuroshio Current centered on  $294^\circ\text{E}$ ,  $39^\circ\text{N}$ . The red curve is the unbiased spectra with the constant noise level removed (horizontal dashed line) from the original spectrum (black curve). (Credits: CLS/CNES and Dufau et al., 2016)

If we look at the averaged 1-Hz, 1-sec data, the spectral “bump” is absorbed into a white noise floor, as shown in the example for Jason in Figure 8.5b (black line) for the energetic Kuroshio Current region. If this noise floor is stable, it can be subtracted as a constant value from the global spectra to reveal the unbiased spectra, showing an ocean signal that decreases more smoothly to smaller scales (red line). Geostrophic turbulence theory predicts a particular slope of the power-law dependence of the spectrum on wavenumber,  $k$ , in a log-log plot, being  $k^{-5}$  in SSH or SLA, and  $k^{-3}$  in surface velocity. Figure 8.5b shows that over the Kuroshio, the SSH spectra are flatter than predicted by geostrophic turbulence.

Different studies have used this technique to estimate how the unbiased spectral slopes vary from one region to another. Figure 8.6 shows the global distribution of spectral slopes of unbiased SSH wavenumber spectra from Xu and Fu (2012) that have a large regional variation. Spectral slopes in the more energetic western boundary regions and the Antarctic Circumpolar current can reach  $k^{-4}$  or  $k^{-4.5}$ , but never the  $k^{-5}$  of geostrophic turbulence theory. Spectral SSH wavenumber slopes are much flatter in the eastern basins and the tropics. The reasons for this discrepancy are being actively explored, but the presence of high-frequency internal tides and internal waves may increase the spectral SSH energy at short wavelengths and flatten the regional spectra (Richman et al., 2012; Rocha et al., 2016; Dufau et al., 2016).

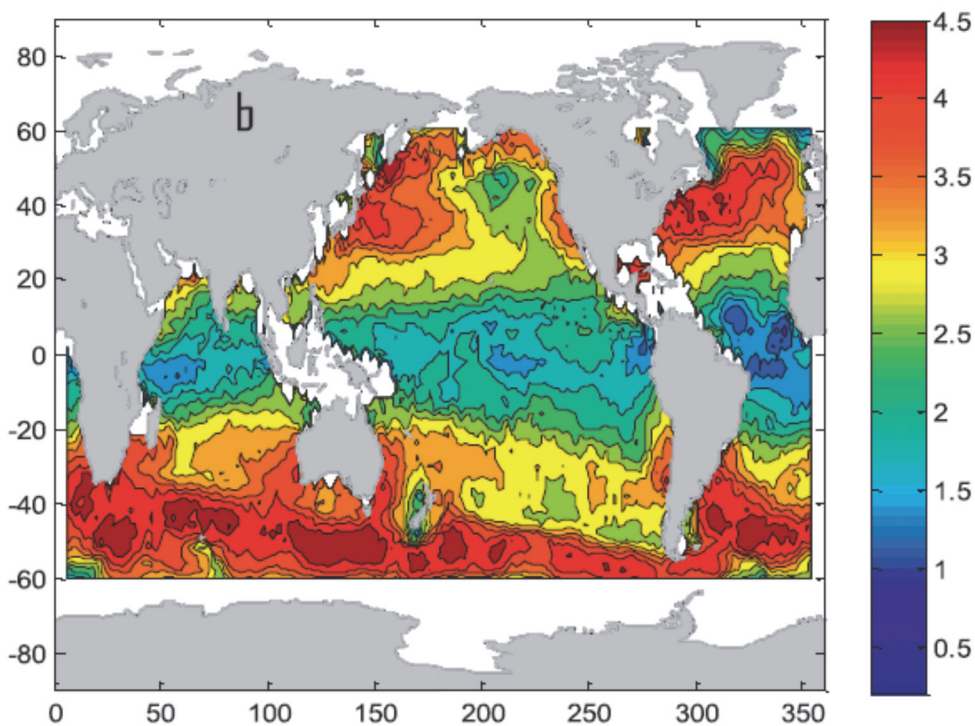


**Figure 8.6.** Global distribution of spectral slopes of unbiased SSH wavenumber spectra over the “mesoscale” band of 70-250 km estimated from Jason-1, after removing the noise. After Xu and Fu (2012).

---

## Major measurement error contributions to SSH at different space-time scales

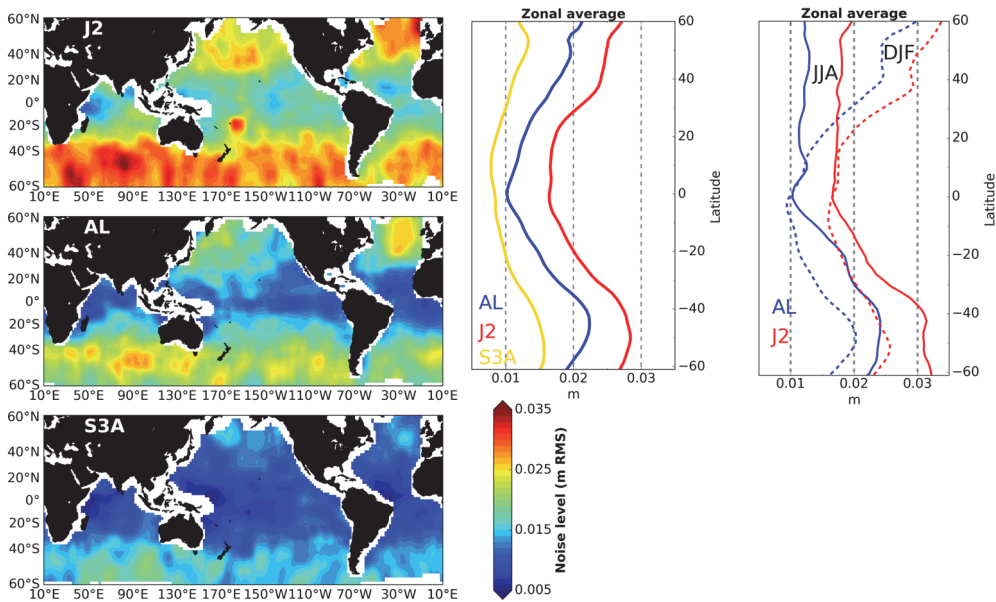
In the previous section, we have seen how the global altimetric spectral noise levels vary from one mission to another. The analysis of along-track SSH wavenumber spectra also allow us to investigate the seasonal and regional patterns of the 1 Hz noise level for each satellite.

Figure 8.7 shows an example of how the altimetric noise levels vary regionally (left) and seasonally (right), based on Jason-2, Saral and Sentinel-3 data (O. Vergara, personal communication). The 1 Hz altimetric noise is estimated from a horizontal straight line fit to the averaged wavenumber spectra from 10-25 km wavelength (see Figure 8.5b). The averaged wavenumber spectra are calculated from all of the edited along-track tracks occurring in  $15^\circ \times 15^\circ$  boxes over the entire period (left) or each season (right). The decreasing instrument noise from Jason-2 to Saral to Sentinel-3 is clearly shown in the zonally averaged values (middle panel). The right panel in Figure 8.7 shows that the highest noise levels occur in winter in both hemispheres. Regions with high noise levels also have a high hump artifact (Dibarboure et al., 2014), i.e., where the altimeter waveforms include inhomogeneity within the footprint due to surface roughness changes, rain cells, etc., that increase the altimeter error level for wavelength between 10 and 25 km. Different techniques have been proposed to reduce this effect in the future using a dedicated data selection (Dibarboure et al., 2014) or by applying a two-step retracking algorithm on Cryosat-2 LRM data (Garcia et al., 2014).

There is a strong seasonal variation in the SSH error level since all factors contributing to the 1 Hz error (significant wave height, rain wells, wind streaks, and ocean slicks) vary seasonally and regionally. Figure 8.7 shows that the maximum SSH error level occurs during winter (December-January-February for the Northern hemisphere, June-July-August for the Southern hemisphere) with higher values in the south (3 cm rms compared to 2.5 cm rms for the north). The dominant contributor to the increased noise in winter is the higher sea-state. Around the Equator, a dipole in the SSH error level is present during winter and summer, with strongest values in the Inter Tropical Convergence Zone (ITCZ) and weak values in the trades wind regions on either side. These higher values are particularly due to rain cells and so-called sigma-0 bloom patches in the ITCZ (Dibarboure et al., 2014).

Another source of errors comes from the mean sea surface (MSS) used, particularly for non-repeat or new orbit missions where the SLAs are calculated with respect to gridded MSS products. Although these MSS products have greatly improved over the last years, including recent geodetic or drifting altimeter missions, MSS errors still impact the altimetric signal over wavelengths less than 100 km. Pujol et al. (2018) showed that MSS errors can explain 30% of the global SLA variance on new or drifting missions (e.g., Sentinel-3) and the error can be 2.5 times higher for unchartered tracks over rough bathymetry.

Many altimetry users apply an altimeter error for each mission that is constant in space and time. In the future, it could be beneficial for users to take into account how the SSH error level is modulated in space and time (e.g., for the assimilation of along-track altimetry in ocean models).



**Figure 8.7.** Left panel: 1 Hz noise levels (in m rms) from different altimeter missions based on mean SSH wavenumber spectra calculated in  $15^\circ \times 15^\circ$  boxes from (top) Jason-2, (middle) Saral, and (bottom) Sentinel-3A. Middle panel: Zonally-averaged noise levels for each mission. Right panel: Seasonal variations in zonally-averaged noise levels for the Jason-2 (red) and Saral (blue) missions for Jun-Jul-Aug (JJA solid) and Dec-Jan-Feb –DJF, dashed). (Credits: O. Vergara, LEGOS)

## Fine-scale altimetry near the coast

A key issue in satellite altimetry is the monitoring of coastal oceans (Vignudelli, et al., 2011). The coastal ocean dynamics have shorter space and time scales and larger SSH amplitudes due to their shallower bathymetry. Narrow coastal currents and tides need to be monitored due to their important socio-economic effects (pollution control, biomass advection, marine safety and shipping, ...). Changing sea level at the coast impacts coastal morphology and erosion occurring over a large range of time scales, including extreme events via storm surges.

The excellent monitoring of the open-ocean dynamics from altimetry is mainly due to the fact that we can resolve the scales of the most energetic mesoscale features (150–200 km). The scales resolved by these gridded maps are not well-adapted to the smaller, faster coastal dynamics. For the along-track data, major problems exist – the footprint size of 200 km<sup>2</sup> for conventional altimetry is very large and averages over different dynamical regimes close to the coast (SARM with 5 km<sup>2</sup> footprint size is better adapted, especially when the ground tracks are perpendicular to the coast). The distance between altimetric ground tracks is also large compared to the smaller space and time scales of the coastal dynamics. In addition, as the along-track altimeter data approaches the coast, the data returned from the radar footprint becomes perturbed by the coast or islands/shallow banks/sea-ice (see Figure 8.8). The standard Brown waveform retracking fails and data is flagged around 10 km from the coast.

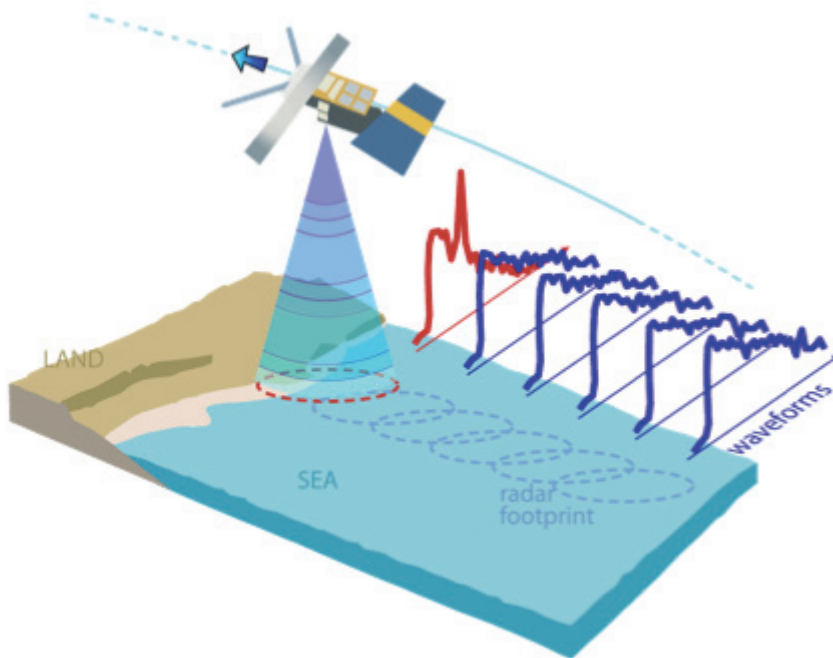


**Figure 8.8.** Schematic of the along-track radar waveforms being perturbed by the presence of land in the footprint. (Credits: ESA)

Additional problems affect the availability and quality of the coastal altimeter data. The radiometer measurements used to derive the wet-troposphere correction becomes perturbed even further from the coast due to their larger footprint at different frequencies, and standard data is lost up to 25-50 km from the coast. Other corrections such as the ionospheric correction or the ocean tides and dynamic atmospheric correction require specific processing or models for the coastal band.

Over the last decade, major advances have extended the capabilities of satellite altimetry for the observation of the coastal circulation and the complex interactions between the coastal and the open ocean circulation. Progress has been made in reducing the altimeter footprints and noise to approach closer to the coast (CryoSat-2- SAR, Saral/AltiKA, Sentinel-3-SAR), but also in processing algorithms, corrections, and products for coastal applications (Vignudelli et al., 2011; Obligis et al., 2011; Fernandes et al., 2014, Birol et al., 2017). The improved coastal altimeter data and their derived sea level and wind-wave data are being integrated into coastal observing systems. These data provide essential monitoring for both research and operational applications in these coastal regions where in situ measurements are sparse.

---

## Future SWOT Mission – 2D Swath SSH Observations

The last 30 years of satellite altimetric studies have greatly advanced our understanding of the large-scale ocean circulation and its interaction with the larger mesoscale dynamics (Fu and Cazenave, 2001; Morrow et al., 2017). We are entering a new period where ocean models are evolving at high-

resolution and global models, with and without tides, are now available (HYCOM at  $1/25^\circ$  - Chassignet and Xu, 2017;  $1/48^\circ$  MITgcm,  $1/60^\circ$  NEMO NATL, etc.). However, the dynamics of these models cannot be validated due to the lack of global observations at these finer scales. The future SWOT SAR-interferometry wide-swath altimeter mission is designed to provide global 2D SSH data resolving spatial scales down to 15-20 km, for a 2 m high significant wave height (Fu et al., 2012; Fu and Ubelmann, 2014); these values vary depending on the sea-state. These observations will fill the gap in our knowledge of the 15-200 km 2D SSH dynamics, important for the ocean horizontal circulation and kinetic energy budget, but also for driving energetic vertical velocities and tracers' transports (Levy et al., 2012).

As the name suggests, the Surface Water and Ocean Topography (SWOT) mission will bring together two scientific communities – oceanographers and hydrologists. For the hydrology community, SWOT SAR interferometric data will enable the observation of the surface elevation of lakes, rivers and flood plains, and will provide a global estimate of discharge for rivers  $> 100$  m wide, and water storage for lakes  $> 250$  m<sup>2</sup>. SWOT will also provide unprecedented observations in the coastal and estuarine regions, of interest to both communities. The science objectives covering all disciplines are outlined in the SWOT Mission Science Document (Fu et al., 2012).

Here, we provide an overview of the SAR-interferometry measurement technique, the chosen orbits and space-time sampling, the ocean science objectives and applications, and the ocean error budget including the impact of waves. We present some of the research studies aiming to understand the new 2D SSH dynamics that will be observed at scales from 15-200 km. In particular, there will be a significant SSH contribution from high-frequency contributions such as tides, internal tides, and internal gravity waves, which are not in geostrophic balance. Observing their regional and seasonal signals and their interactions will be a great achievement for SWOT. A challenge is in separating the balanced motions from the high-frequency signals in order to calculate geostrophic velocity or vorticity. The spatial sampling is excellent, but weaker temporal sampling presents a challenge in mapping the high-resolution 2D “snapshots”. We discuss the new 2D and 3D mapping techniques being developed for SWOT swath data. Finally, we present some early studies on assimilating SWOT simulated SSH data in operational ocean models.

---

## Principle of SAR in SWOT measurements

Interferometric Synthetic Aperture Radar (InSAR) has been used extensively during the past three decades for fine-resolution mapping and measuring changes of the surface of the Earth. The principle is to combine two SAR images of the same place on the ground taken from two distinct positions of the radar  $A_1$  and  $A_2$  separated by a distance  $B$  called the baseline (see Figure 8.9). Figure 8.9 is drawn in the plane orthogonal to the satellite speed vector, the line  $A_1, A_2$  is then in the across-track direction. This explains the name cross-track interferometry.

In the past, the two images were standard SAR images taken at two different times for successive overflights of the same region by the same radar. The incidence angle (or look angle  $\theta$  shown on Figure 8.9) was typically between 20 and 40 degrees. In the case of SWOT, the satellite carries two antennas and then the two images can be obtained simultaneously. One other important difference

is that the look angle  $\theta$  is much lower (between  $0.6$  and  $4^\circ$  for SWOT), so these measurements are quasi-nadir SAR interferometry. This has some noticeable effects that are discussed at the end of this section.

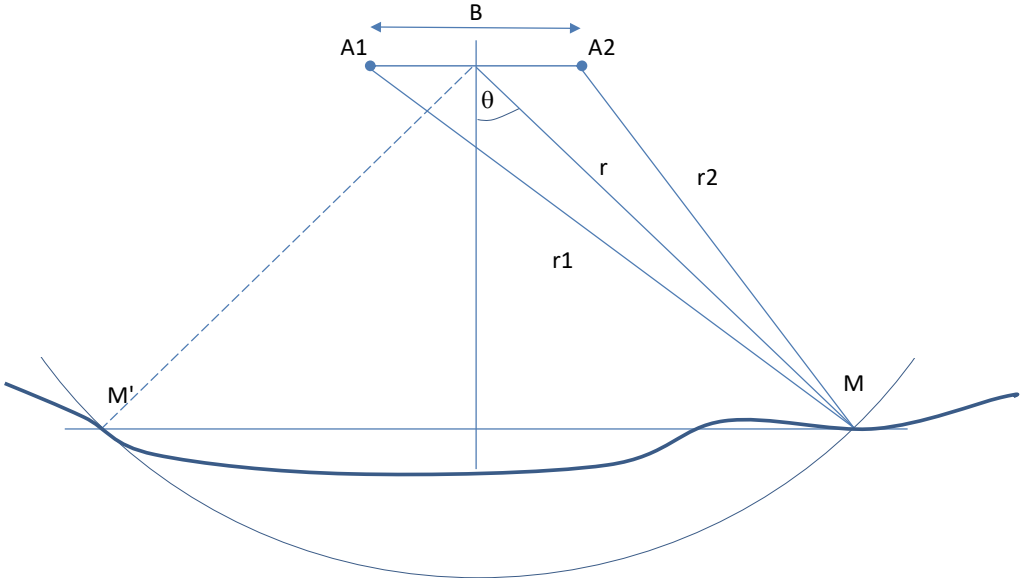


**Figure 8.9.** Principle of cross-track interferometry. After Frappart et al. (2017).

The two radar measurements can be used to determine the range  $r_1$  and  $r_2$  with a range resolution of around one meter (0.75 meter for SWOT). However, the instruments also measure the phase of the signal, and the interferometric phase  $\Phi$  can be computed for each bin of the interferogram line (which is analogous to the waveform defined in nadir altimetry).

$$\Phi = \phi_1 - \phi_2 = 2\pi \frac{r_1 - r_2}{\lambda} \quad (2\pi) \tag{2}$$

where  $\lambda$  is the wavelength of the electromagnetic wave emitted by the altimeter.

This measurement is made with great accuracy but the phase difference between the two return signals has an ambiguity of  $2\pi$ , which is removed by a processing called phase unwrapping (Rodriguez et al., 2017). After phase unwrapping, the absolute phase  $\Phi_a$  is known and the differential range  $r_1 - r_2$  can be deduced from it.

$$\Phi_a = 2\pi \frac{r_1 - r_2}{\lambda} \tag{3}$$

The incidence angle  $\theta$  can also be computed from the knowledge of  $\Phi_a$ .

$$\Phi_a = \frac{2\pi}{\lambda} B \sin(\theta) \tag{4}$$

Then, knowing the range  $r$  and the angle  $\theta$ , the position in 3D space of the point M can be obtained. This process is called geolocation and height retrieval. This is a very simplified description; again, further details are given in Rodriguez et al. (2017).

When the surface is flat enough (such as over the ocean) and the backscattering is almost uniform, the SWOT measurements can be used to retrieve water heights from each line of the interferogram. This provides a height profile in the plane of Figure 8.9. The measurement is repeated

with a high frequency, and assembling the successive profiles allows the processor to build an image of the surface height over the swath width of 50 km (see Figure 8.10).

The processing of the image formation is done independently for the left and the right swaths of SWOT. Note that if the point  $M'$  is symmetrical with  $M$  in respect to the vertical line passing by the middle of the two antennas, then  $M'$  is measured at the same range as the signal coming from  $M$  (Figure 8.9). This leads to an ambiguity in the detection of signals coming from the left and right swath that has to be removed at the instrument level. For SWOT, this is done using the right and left antenna patterns and using different polarization of the signals (one pulse is emitted in H-polarisation, the next in V-polarisation, etc.). For InSAR on CryoSat-2 used over the polar ice-caps, the goal was to provide measurements at nadir and there is no device to remove the left-right ambiguity. So, Cryosat-2 InSAR observations are not well-adapted for flat ocean observations. However, if the incidence angle on the ground is very different on the left and right sides (e.g., in the presence of steep terrain slopes in the cross-track direction on a polar ice-cap), then the radar-returned power on one side is close to zero. Consequently, the return signal is considered to come only from one side only, removing the left/right ambiguity. In these cases, the near-nadir CryoSat-2 SAR interferometer measurement can identify the direction of the main signal and then obtain both a height measurement and position.

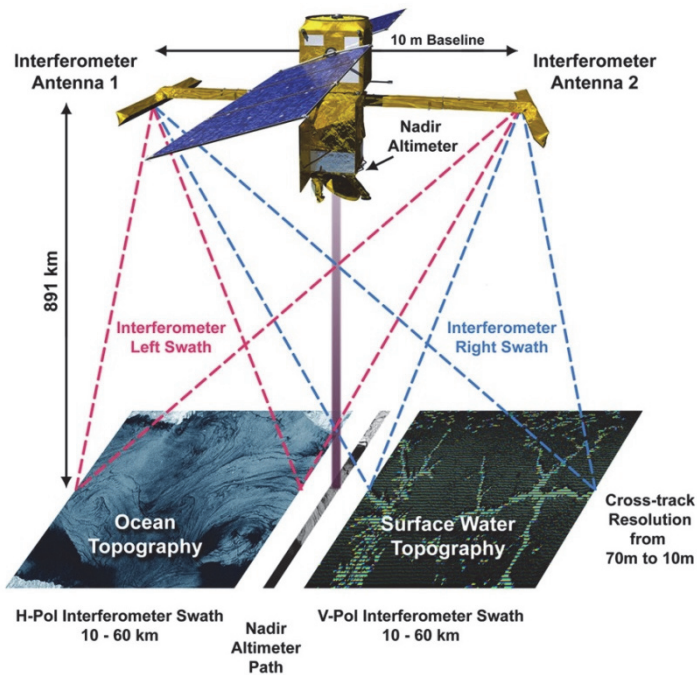


**Figure 8.10.** Schematic of the SWOT measurement technique using the KaRIn instrument for SAR-interferometry over the two swaths, and a Jason-class nadir altimeter in the gap. (Credits: NASA-JPL)

SWOT uses SAR processing to refine the along-track resolution of the return signal, as explained in the second section of this chapter. The interferometric processing refines the cross-track resolution. The SWOT SAR-KaRIn instrument provides a basic measurement resolution of

2.5 m along-track, and ranges from 70 m in the near-nadir swath to 10 m in the far swath. Over the terrestrial water surfaces, an onboard pre-summing is performed and data are downloaded at 5.5 m resolution along-track, with the maximum cross-track resolution. Full interferometric processing is then performed on the ground. Over the 70% of the Earth's surface covered by the oceans, the huge amount of data being produced cannot be downloaded from the satellite. Instead, so-called "low-resolution" data are pre-processed onboard and building blocks of nine interferograms at 250 m posting (and 500 m resolution) are downloaded from each antenna. Other parameters that are useful for the surface waves and front detection, such as the 250 m resolution backscatter images, are also downloaded. These data are combined through the geolocation and height calculation into a 250 m x 250 m expert SSH product with higher errors in swath co-ordinates, and a standard 2 km x 2 km product in along-swath and geographically fixed coordinates. The error estimate of these averaged data is 2.25 cm/km<sup>2</sup>, more than an order of magnitude smaller than conventional Jason-class measurements.

---

## SWOT Orbit coverage and space-time sampling

The SWOT Science Definition Team investigated the SWOT nominal orbit coverage in detail. Any orbit choice is a trade between good spatial coverage and temporal coverage, but not both. The two major communities using SWOT observations had different objectives – the hydrologists needed global coverage of the smallest lakes and rivers, including at the Equator, on a monthly time scale. The oceanographers needed to cover the small ocean scales evolving rapidly – yet full space and time coverage is not possible with one satellite. The final orbit was chosen to cover most of the terrestrial surface waters and oceans up to 78°N and S (inclination of 77.6°) at 890.6 km altitude on a 21-day repeat orbit, allowing near-global coverage after the full cycle (see Figure 8.11b). SWOT has a non-sun-synchronous orbit and its inclination and repeat sampling were specifically chosen to resolve the major tidal constituents, particularly important to resolve the coastal tides, the high-latitude tides, and to advance on the observation of internal tides.

The orbit has a one- and ten-day sub-cycle, with a westward coverage of tracks. Figure 8.11a shows how the tracks are laid down after three days. One day of coverage loosely covers the globe with big gaps between the swaths (one-day sub-cycle), then successive tracks are laid down to the west leaving a gap of approximately one swath at the equator, but helping to monitor the predominant westward propagation of mesoscale instabilities. After ten days, the whole globe is covered (the ten-day sub-cycle) and over the next ten days, the entire pattern is laid down again, but shifted westward to fill in the small holes between tracks. This satisfies the hydrologists with complete global coverage and gives the oceanographers good global coverage every ten days. Given the overlapping swaths, local coverage at certain latitudes is observed more frequently (two to four times at mid-latitude, up to seven times at high latitude).

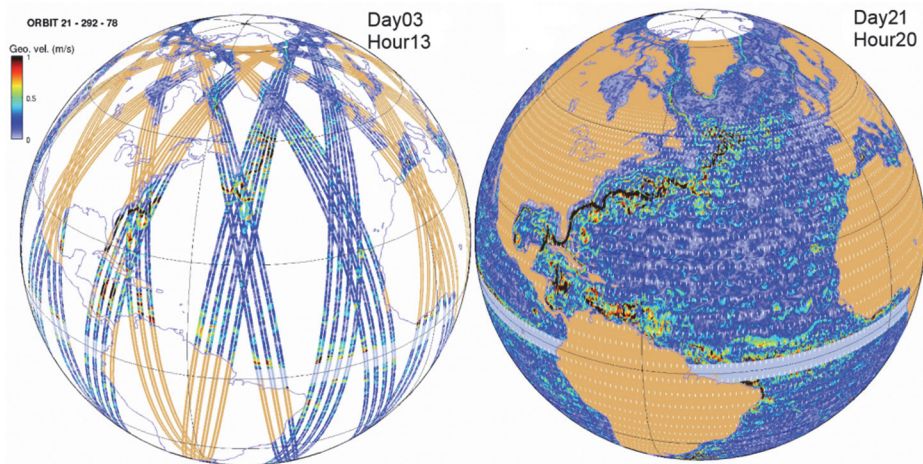


**Figure 8.11.** SWOT’s nominal orbit coverage up to 78°N and S after a) 3-days and b) the full 21-days of a complete cycle. Color shows the evolving simulated along-track geostrophic currents for each track. (Credits: C. Ubelmann, CLS)

After the launch planned for 2021, SWOT will spend six months in the so-called “Calibration orbit,” where the satellite passes over the same site every day to calibrate the satellite parameters. The first three months of this orbit will be to adjust and calibrate the instrument parameters, the second three months will be available for science studies, including studies of rapidly evolving small-scale ocean dynamics. SWOT will then continue in the nominal 21-day repeat orbit for three years, from 2021 to 2024. Details of the nominal and calibration orbits in different formats are given on the AVISO website: <https://www.aviso.altimetry.fr/en/missions/future-missions/swot/orbit.html>.

---

## SWOT error budget

As discussed in the previous section, the noise level is important as it will limit the observation of small scale ocean dynamics. The SWOT SAR-interferometry measurement is designed to have small instrument noise to meet the stringent requirement of 2.25 cm<sup>2</sup>/km<sup>2</sup> noise over the oceans at short wavelengths, for a 2 m SWH average sea-state. This is calculated over 1 km x 7.5 km averages (to resolve the 15 km Nyquist wavelength). For comparison, the noise level for the Jason series is around 100 cm<sup>2</sup>/km<sup>2</sup> at 1 Hz, i.e., averaged over the 1 sec oval footprint or roughly 100 km<sup>2</sup>. The SWOT instrument measurement will be very, very precise! For the first time for an altimetric mission, the error budget is also set in terms of wavenumber, so the instrument design must meet long wavelength and short wavelength goals. SWOT needs to account for standard altimetric SSH range errors, but in wavenumber space. SWOT also has specific errors associated with the interferometric calculation, which are detailed in the SWOT Error Budget and Performance document (Esteban Fernandez, 2017) and in Rodriguez et al. (2017). These include:

- Roll errors. The largest error source for swath altimeters, due to the platform roll, which is minimized by having a stiff mast. This error is linear in the cross-track direction and is estimated by crossover calibration.

- Phase error. This has the effect of moving the estimated height along an iso-range line, and is similar to the roll error but with less magnitude. Phase errors can be random, e.g., due to thermal noise, or systematic; systematic errors can be induced by mismatches in the path lengths of the two channels, temperature changes, or differences induced by the antenna patterns and baseline structures.
- Range errors. These errors also occur in along-track altimetry, including orbit errors; atmospheric propagation errors, including the wet and dry tropospheric errors, ionospheric errors; errors in the geophysical corrections: tides, dynamical atmospheric correction, sea state bias, etc.)
- Baseline errors. An error in the baseline (mast) length results in a height error. This is estimated to be very small.
- Radial velocity errors. To have good geolocation with SAR processing, one needs good knowledge of the radial component of the relative velocity between the satellite and the surface. Any mean error in this radial velocity will induce a horizontal displacement of the moving target and an error in the position (and geolocation).
- Wave effects. The combination of the near-nadir incidence of SWOT and moving surface waves leads to several effects, which are detailed in Peral et al (2015) and Rodriguez et al; (2017). These include a “surfboard” effect, where the waves are sampled multiple times leading to distortion of the waves’ height and spatial distribution. A second “wave bunching” effect is due to the wave scatterers on a moving surface sending back different magnitudes and signs, leading to a non-linear distortion of the surface. Interferogram averaging can help suppress the wave-bunching effect from leaking into the sub-mesoscale range.
- EM bias. This bias is induced by modulations in the surface brightness that lead to a net lowering of the mean surface

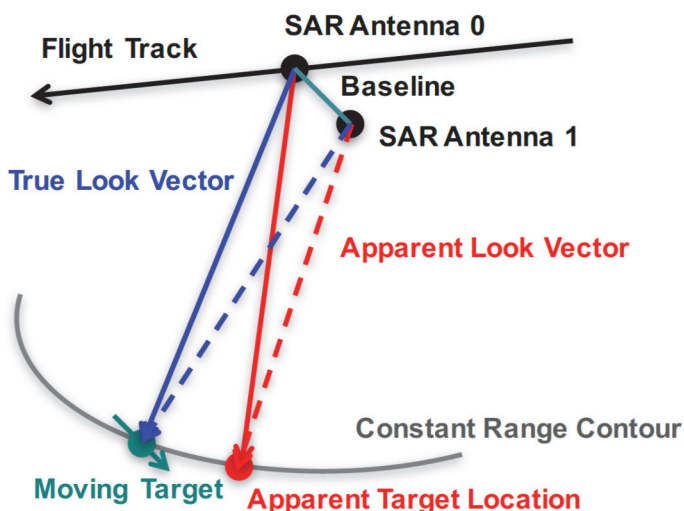


**Figure 8.12.** Schematic of the apparent shift of a moving target on the ocean along constant range lines, causing a small error in the interferometric height estimate. After Rodriguez et al. (2017).

An example of the impact of radial velocity effects from a moving target (such as surface waves) is shown in the schematic in Figure 8.12. Any moving targets on the ocean surface appear shifted in SAR images. Without knowledge of the target motion (and a correction for it), the difference between the interferometric phase between the target's true and apparent position becomes an interferometric height error. For SWOT over the oceans, the pointing control error is small and the velocity errors from surface waves are thus small, and are included in the error budget.

The breakdown of all of these errors in terms of their wavenumber spectral density is shown in Figure 8.13, from the SWOT Error Budget and Performance document by Esteban-Fernandez (2017). The largest error source is from the KaRIn instrument errors, the random errors dominating at scales  $< 100$  km, gyro and systematic errors dominating the large scales.

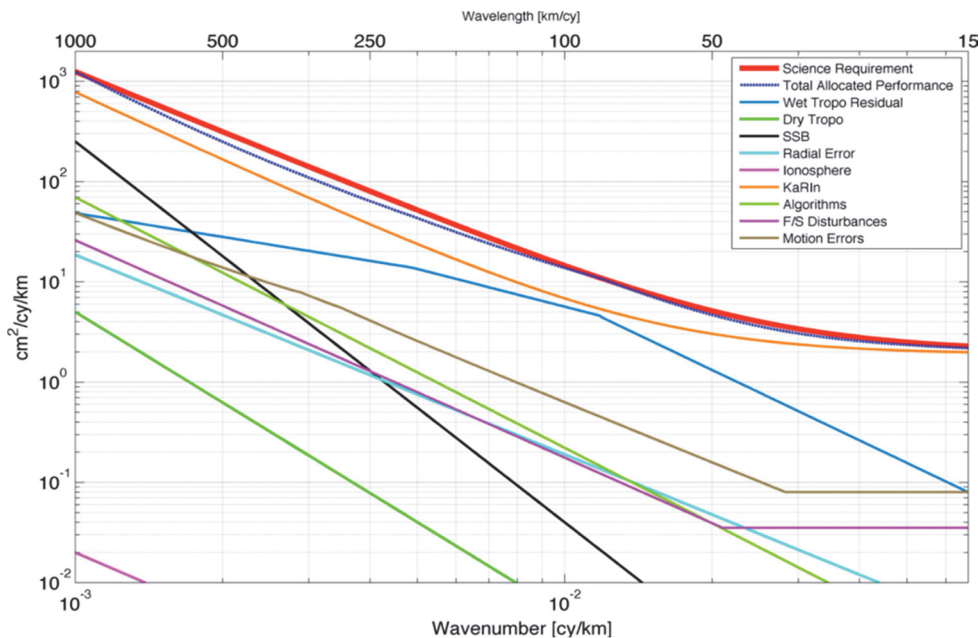


**Figure 8.13.** Wavenumber spectral estimates of the different components of the SWOT error budget for wavelengths  $< 1000$  km. After Esteban-Fernandez (2017).

## New 2D SSH dynamics observed at scales from 20-200 km

The primary oceanographic objective of the SWOT mission is to characterize the ocean mesoscale and submesoscale circulation determined from the ocean surface topography at spatial resolutions down to 15 km wavelength. Current altimeter constellations can only resolve the 2D ocean circulation at resolutions larger than 200 km.

Although the larger mesoscale eddies have been tracked and analyzed with standard altimetry maps (e.g., Chelton et al., 2011), these eddies “spontaneously” appear and disappear in mid-ocean and, at present, we cannot observe the smaller-scale processes that create the larger eddies, nor their cascade down to smaller dissipative scales. Recent high-resolution modelling has highlighted the importance of the smaller scales generated, for example, by energetic instabilities in the deep winter mixed layers. Figure 8.14 shows a comparison of winter and summer surface relative vorticity (the

Laplacian of SSH – upper panel) and upper ocean vertical velocities (lower panel), derived from the  $1/48^\circ$  Earth Simulator model for the North Pacific, with no tides (Sasaki et al., 2014). The late winter surface relative velocity shows a myriad of small-scale structures and filaments associated with strong vertical velocities at small-scales in the deep winter mixed layer, and some injection into the sub-surface layers (left panels). In late summer, when the mixed layer is rather shallow, the near-surface vertical velocities are quite weak, and the surface relative vorticity is less energetic and at larger scales (right panel). These processes are mainly in geostrophic balance and have a SSH signature that should be detected by SWOT.

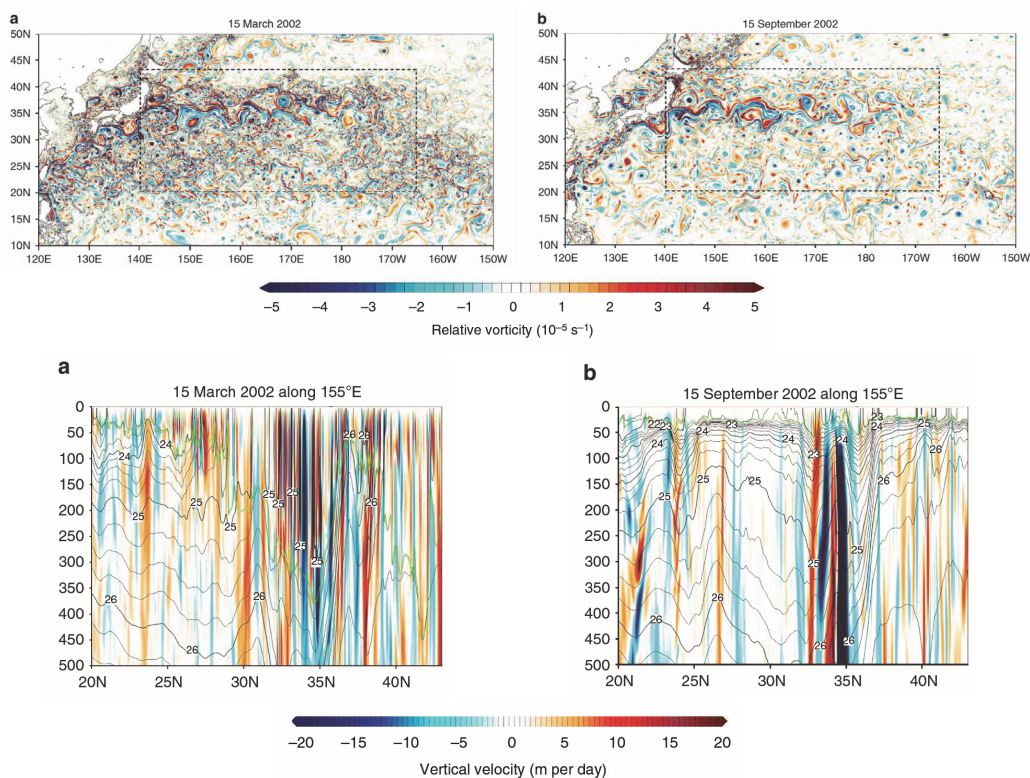


**Figure 8.14.** Upper panel: Surface relative vorticity in the Northwestern Pacific on (left) March 15, in winter and (right) September 15, 2002, in late summer. Lower panel: model vertical velocity along  $155^\circ\text{E}$  for both dates. The depth of the mixed layer is marked by the green contour. After Sasaki et al. (2014).

### Kinetic energy and tracer transports

Global study of the circulation at scales of 15 -200 km is essential for quantifying the kinetic energy of ocean circulation and the ocean uptake of heat and carbon that are key factors in climate change. Exchange of heat and carbon between the ocean and the atmosphere is regulated by the large-scale mean circulation, as well as by the mesoscale and submesoscale eddies. Traditional altimeters combined with in situ data have revealed the fundamental role of mesoscale eddies in the horizontal transport of heat and carbon (Dong et al., 2014). The uptake of heat and carbon by the ocean is complete only after the vertical transport process from the surface turbulent boundary layer into the ocean interior is accomplished. The vertical transport is mostly accomplished by the submesoscale

fronts with horizontal scales 15-50 km (e.g., Lévy et al., 2012). The SWOT mission will open a new window for studying the SSH signature of these processes.

The transfer of kinetic energy between the different dynamical scales is also of interest. Figure 8.15 also from Sasaki et al. (2014) shows the temporal evolution of the surface kinetic energy (KE) field, which is mainly in geostrophic balance at these scales. The KE field has been filtered to reveal the small-scale motions less than 200 km (in black) and the larger scales in red and blue, which are resolved today by gridded altimetry data. The peak in KE in winter is associated with the energetic small-scale mixed layer instabilities seen in Figure 8.14. Calculations on the transfer of energy reveal that the small-scale processes < 100 km wavelength peak in late winter Mar-Apr; these then feed energy up to the larger mesoscales that develop over time, with scales of 100-200 km peaking in Apr-May and 200-300 km peaking in early summer June (in red). With conventional altimetry maps, only the scales greater than 200 km are observed and the seasonal cycle is biased towards the summer peak, with no observations of the small-scale generating mechanisms in winter. These model results need to be validated by 2D observations, which will be available from the SWOT mission.

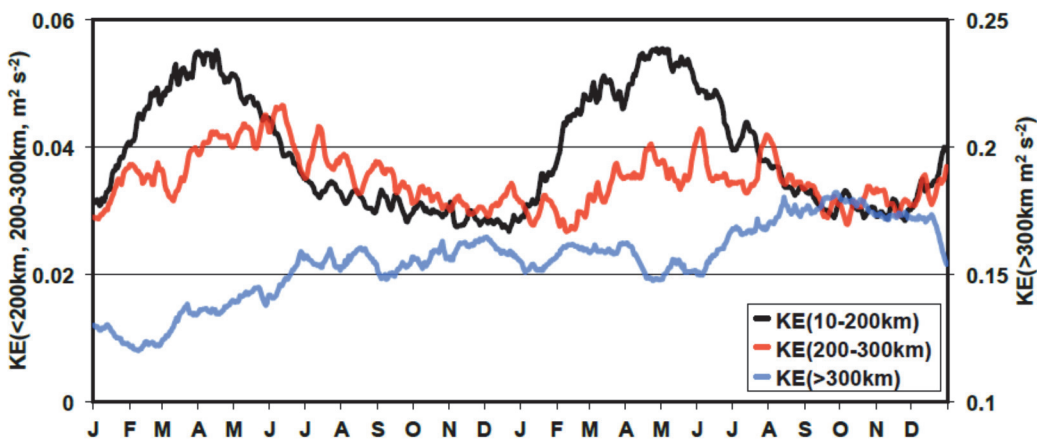


**Figure 8.15.** Kinetic energy in the 10-200 km band (black), in the 200-300 km band (red) and for scales > 300 km (blue) calculated over a two-year period in the box 20-43°N, 148°E-168°W from the Earth Simulator. After Sasaki et al. (2014).

### Climate change and ocean circulation

The new knowledge of the KE of the ocean circulation and the vertical transport of carbon and heat is crucial for understanding the role of the ocean in regulating climate change through the interaction of the mesoscale and submesoscale variability with the large-scale circulation. Accurate knowledge of the large-scale circulation is thus also required to achieve these objectives, posing a requirement on measurement accuracy from the submesoscale to the global scale. For this, SWOT will carry a nadir altimeter positioned between the two swaths (see Figure 8.10), providing accurate SSH monitoring of the larger mesoscales and large scale circulation simultaneously with the 2D KaRIn observations of the smaller scales.

### Coastal ocean dynamics

Coastal ocean dynamics are important for many societal applications. As mentioned earlier, they have smaller spatial and temporal scales than the dynamics of the open ocean and require finer-scale monitoring. SWOT will provide global, high-resolution observations of 250 m to 2 km resolution right up to the coasts, for observing coastal currents and storm surges. While SWOT is not designed to monitor the fast temporal changes of the coastal processes, the swath coverage will allow us to characterize the spatial structure of their dynamics when they occur within the swath.

Figure 8.16 shows the winter-time relative vorticity for the MARS model in the Bay of Biscay, with energetic fine-scale structures near the coasts and at the shelf edge, under the influence of density gradient instabilities from the freshwater river plumes and tidal mixing. The continuum from the regional seas to the shelf, to the nearshore region and into the estuaries involves complex coastal dynamics, and SWOT will help monitoring these exchanges over the 3.5 years of observations.

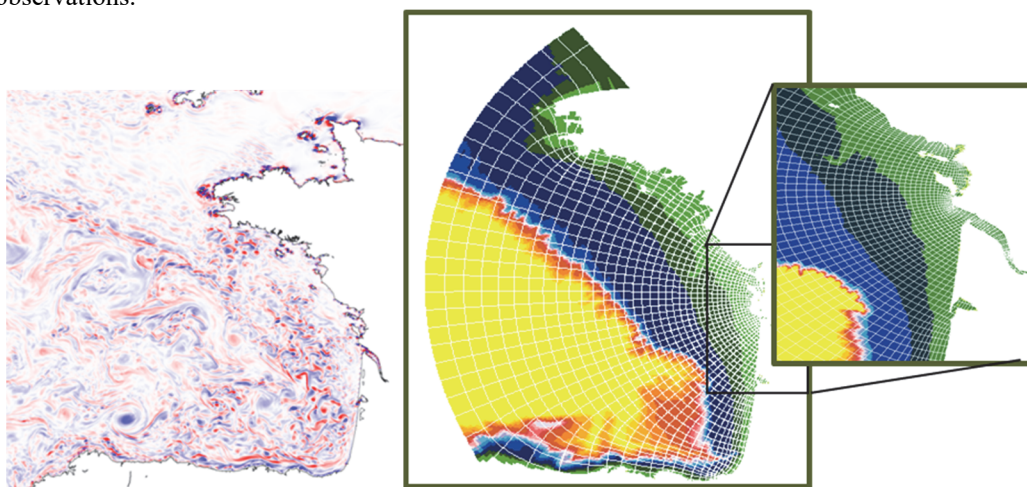


**Figure 8.16.** (left) winter-time relative vorticity in the Bay of Biscay from the MARS ocean model. (right) a hierarchy of embedded models using the Symphony code, with increased resolution towards the coast and into the estuaries. (Credits: N. Ayoub, LEGOS)

---

### High-frequency contributions to SSH at 20-200 km: coastal tides, internal tides and internal gravity waves

The choice of orbit for SWOT is specifically designed to resolve the eight major tidal constituents. Although the Jason series of satellite altimeters has greatly improved our observations (and assimilation into tide models) of the open ocean barotropic tides (Stammer et al., 2014), the short spatial scales of the coastal tides and their non-linear constituents have been harder to monitor, since we miss information in between the Jason tracks. SWOT with its 250 m resolution 2D coverage can be used as a tide gauge at each grid point, with a time series over a three-year period. This should allow unprecedented coverage of the coastal tides and open-ocean barotropic tides, extended up to high latitudes of 78°N and S. Note that the precise historical Jason tidal observations only reach 66°N and S; and the sun-synchronous orbits of the higher-latitude altimeters (ERS, Envisat, Cryosat, Saral) cannot accurately resolve all of the tidal constituents, especially S2.

The new capability of mapping SSH down to 15 km scales will greatly improve our observation and understanding of internal tides that have a small signature in SSH. Internal tides result from the interaction of the barotropic tide with strongly sloping bathymetry in a stratified ocean. They create large amplitude internal waves at the thermocline (10–30 m), leading to small SSH signatures (1–3 cm). They can already be detected in one direction from along-track altimeter data (Ray and Zaron, 2016). SWOT with its lower noise and 2D coverage should provide the first global observations of these internal tides. Figure 8.17 shows the global internal tide M2 amplitude estimated from 20 years of along-track T/P-Jason data and the HYCOM model forced by the M2 tide. Although we have a good idea on how and where these internal tides are generated (Figure 8.17), where they are dissipated remains a crucial question. The interaction of the internal tide with the ocean circulation and currents has been shown to be complex, with ocean currents refracting and dissipating the tide (Ponte and Klein, 2015). The dissipation of the internal tide is estimated to have an important influence on the ocean’s energy budget and the mixing of water masses (e.g., Munk, 1966), but we lack observations to validate this. Knowledge of the 2D energy fluxes in an ocean with internal tides is a key issue that may be addressed with SWOT.

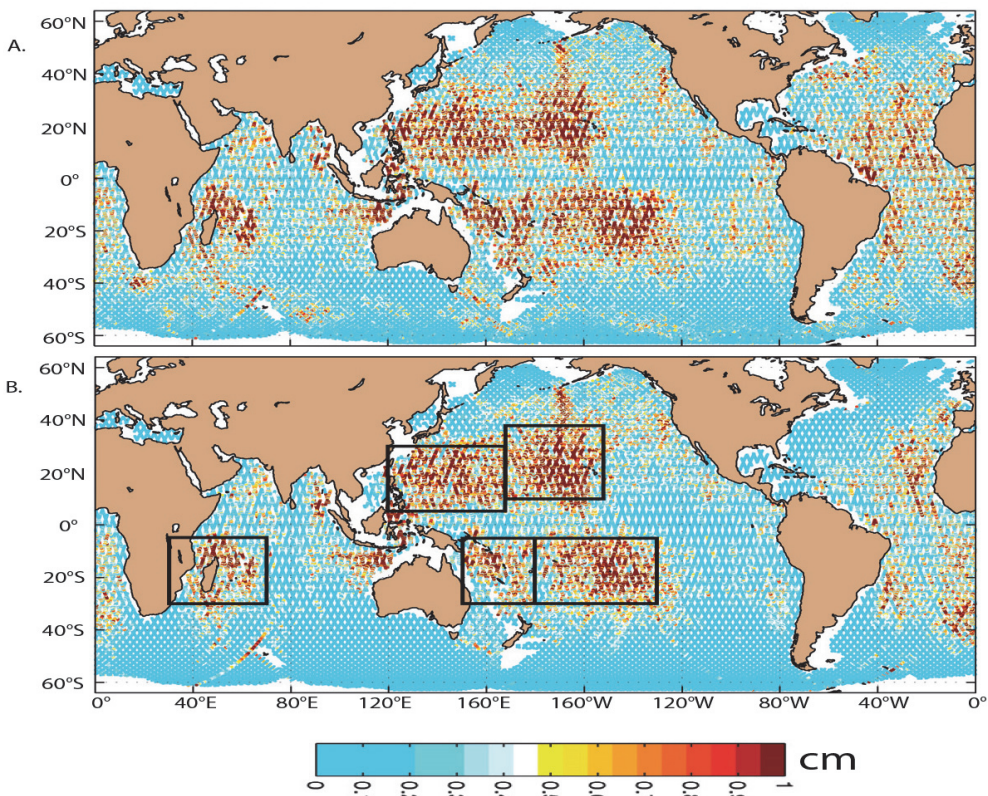


**Figure 8.17.** Amplitudes (top, altimetric and bottom, HYCOM model) of the M2 internal tide signature in sea surface elevation along altimeter tracks. HYCOM output is interpolated to altimeter tracks for comparison. HYCOM simulation is a 32-layer, wind-, buoyancy-, and M2- forced simulation. For both subplots, the internal (baroclinic) tide amplitudes are computed after removing the barotropic M2 signal. After Shriver et al. (2012).

So, these new SWOT observations will not only be crucial for achieving the ocean circulation objectives by separating barotropic and internal tidal signals from circulation signals, but will also be important for applications in both coastal and open oceans (such as navigation, surface drift, pollution control, etc.) and improved understanding of ocean mixing in the coastal and open ocean.

In addition to internal tides, internal gravity waves can be generated in a stratified ocean by the interaction of currents with bathymetry or by localized atmospheric forcing (Garrett and Munk, 1979). Conventional along-track SSH measurements are too noisy to allow direct estimation of the SSH wavenumber spectrum in the 10-80 km wavelength range where internal waves and submesoscale variability co-exist. Both should be apparent in the along-track SAR and 2D SWOT data, and disentangling the two is an important and interesting research challenge. Numerical simulations are starting to produce realistic internal-wave fields (e.g., Richman et al., 2012; Muller et al., 2015; Rocha et al., 2016) that can be used to analyze the relative contributions of internal waves and lower-frequency variability.

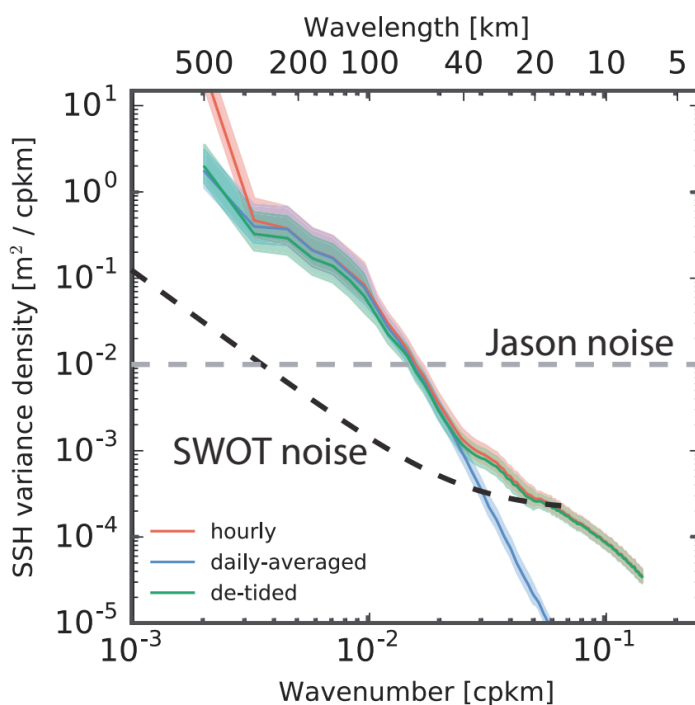


**Figure 8.18.** Wavenumber spectra of SSH in the Drake Passage region from a  $1/48^\circ$  ocean MITGCM model that represents internal waves and geostrophic variability down to scales of 5 km. The difference between SSH wavenumber spectra of hourly model output (red line) and daily-averaged output (blue line) gives an indication of the contribution of variability at periods of two hours to two days, which is expected to be largely due to internal waves. At wavelengths larger than 50 km in Drake Passage, the low-frequency variability dominates the SSH variability (and hence the blue curve and the red curve are almost the same); at scales smaller than 40 km, the high frequency variability from internal waves becomes larger than the low-frequency variability. After Morrow et al. (2017), modified after Rocha et al. (2016).

Figure 8.18 shows wavenumber spectra of SSH in the Drake Passage region from a  $1/48^\circ$  ocean general circulation model that represents internal waves and geostrophic variability down to scales as small as 5 km (figure modified from Rocha et al., 2016). The model output was from the MITgcm

forced by realistic high-frequency wind and tidal forcing (see Rocha et al., 2016). By filtering the model output in time, one can crudely separate the variability at internal wave frequencies (from minutes up to the inertial period, which is about 14 hours in Drake Passage) from the lower frequency variability that is expected to be in geostrophic balance. Comparison of the SSH wavenumber spectra of hourly model output and daily-averaged output gives an indication of the contribution of variability at periods of two hours to two days, which is expected to be largely due to internal waves (Figure 8.18). In Drake Passage, on wavelengths larger than 50 km, the low-frequency variability dominates the SSH variability; at scales smaller than 40 km, the high frequency variability dominates. Figure 8.18 also shows the estimated noise levels for Jason (100  $\text{cm}^2/\text{cycle}/\text{km}$ , e.g., Fu and Ubelmann, 2014) and SWOT (from the SWOT Science Requirements)—the dominance of internal waves begins to occur at the wavelengths that will be newly accessible with the much lower noise levels of SWOT. Recent studies by Qiu et al (2017) analyzing Acoustic Doppler Current Profiler data in the Pacific show that the scales where internal waves become important is geographically variable, and longer wavelengths are affected in the tropics and in low eddy energy regions.

SWOT has the potential of providing the first global SSH observations of the combined geostrophically-balanced flow and the internal wave field, and how they vary both geographically and seasonally and how they interact. Disentangling the two contributions will also be a major challenge, for the future SWOT data and also the fine-scale along-track data.

---

## New 2D and 3D mapping techniques for SWOT swath data

The small-scale features we are starting to detect with the improved along-track altimetry data and with the future SWOT mission are also characterised by their rapid temporal evolution. This presents a challenge since the along-track SAR or SWOT altimetry are providing high spatial resolution but poor temporal resolution (ten-, 20-, 35-day repeats for along-track data; ten-day swath coverage for SWOT). The orbit characteristics of SWOT shown in Figure 8.11 highlight that small, rapid structures will be well sampled for a few days, then re-sampled ten days later, but we cannot observe their temporal evolution.

This dilemma can be illustrated from Figure 8.19. On the left panel, we see 21-days of SWOT swath coverage off the California coast when the simulated noisy SWOT data are just combined, with no interpolation or model advection. The right panels show a series of images based on optimal interpolation (OI) of a true modelled scene of SSH (upper panels) and velocity (lower panels), and a reconstructed scene at the same date from SWOT-like sampling and along-track nadir sampling (Gaultier et al., 2016). In both cases, the distance between the neighbouring tracks or swaths is the limiting factor if we want to ensure a smooth evolution of the flow field. When standard OI is applied after noise removal, we see that the SWOT sampling still retains more anisotropic structure in the SSH field, which gives more energetic currents than with OI applied to the nadir sampling. However, the detailed small-scale eddies and filaments have been smoothed away by the interpolation.

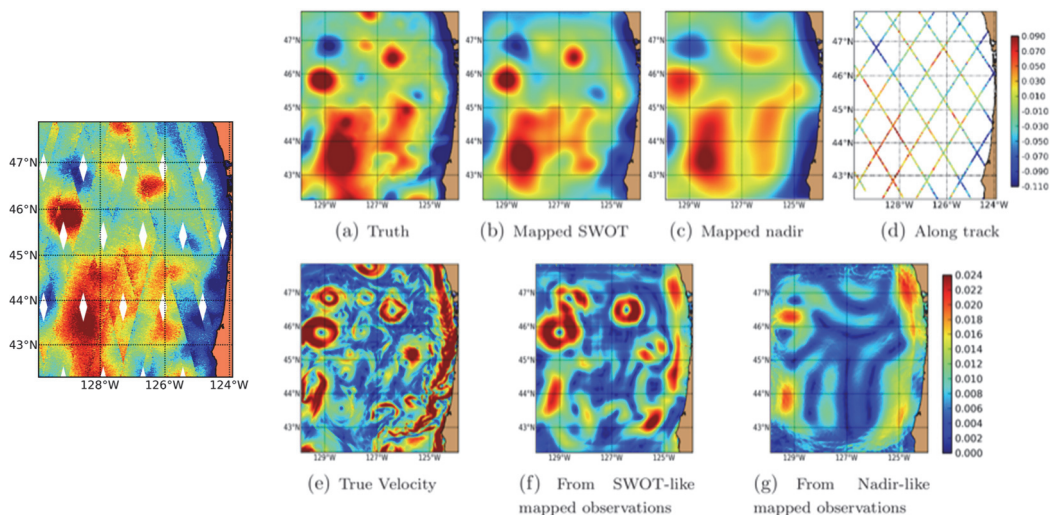


**Figure 8.19.** (Left): SWOT swath coverage off the Californian Coast with simulated SSH and noise over all tracks during a 21-day period. The SWOT modelled SSH is from the MITGCM. (Right): Upper panels: SSH on one date from MITGCM (Truth), interpolated using SWOT-like sampling, using nadir-like sampling, and along-track nadir SSH coverage. SSH in m. Lower panels: same fields in geostrophic velocity (in m/s). After Gaultier et al. (2016).

The first issue to address before mapping the swath data is the noise removal. Figure 8.19 (left) shows simulated SWOT data with the noise from the different error sources added. Simulated SWOT sampling and noise levels are available for ocean studies using a portable tool (not the full instrument simulator) in open source at: <https://github.com/SWOTsimulator/swotsimulator.git>. Since the total SWOT error has different causes and space-time structure, techniques are being developed to estimate the noise using cross-spectral methods (Ubelmann et al., JAOT, submitted) or advanced denoising techniques (Cosme et al., 2017, submitted). This is needed since any ocean studies requiring velocity or vorticity calculations will amplify the small-scale noise when taking the first or second derivatives of SSH.

The second issue is whether a linear statistical model (such as OI) is appropriate to describe the rapid evolution of the smaller eddies and fronts. An example of this problem is shown in Figure 8.20. The upper panels show the SSH evolution over a 300 km x 300 km box covering a large meander, but with several small eddies embedded that should be resolved with SWOT. These eddies move rapidly over this four-day period around the meander. If a linear interpolation is used between days zero and four (equivalent to OI over short time scales), the reconstructed field at day two (lower panels, left) places the large slow meander well, but the small eddy marked with a ‘+’ has not been carried with the flow. Instead it is split into two weak eddies at the original and final positions with half the energy. Ubelmann et al. (2015) proposed instead to use a simple dynamical interpolation based on a nonlinear quasi-geostrophic model with one active layer and the conservation of potential vorticity. For most of the ocean, the first baroclinic mode explains most of the SSH evolution (Wunsch, 1997), so one active layer at fine-scale allows a good reconstruction over short time scales (< ten days). The bottom panels (right) show that the large meander and the small eddy have been correctly positioned with the dynamical interpolation, with greatly reduced errors. This simple dynamical interpolation works well when the lateral advection dominates other

forcing terms, such as air-sea fluxes, and is able to retrieve gridded maps with wavelengths smaller than 100 km over a ten-day window in a mid-energy region (Ubelmann et al; 2015), and down to 60 km in the Mediterranean with weaker energy and smaller scales (Roge et al, 2017).

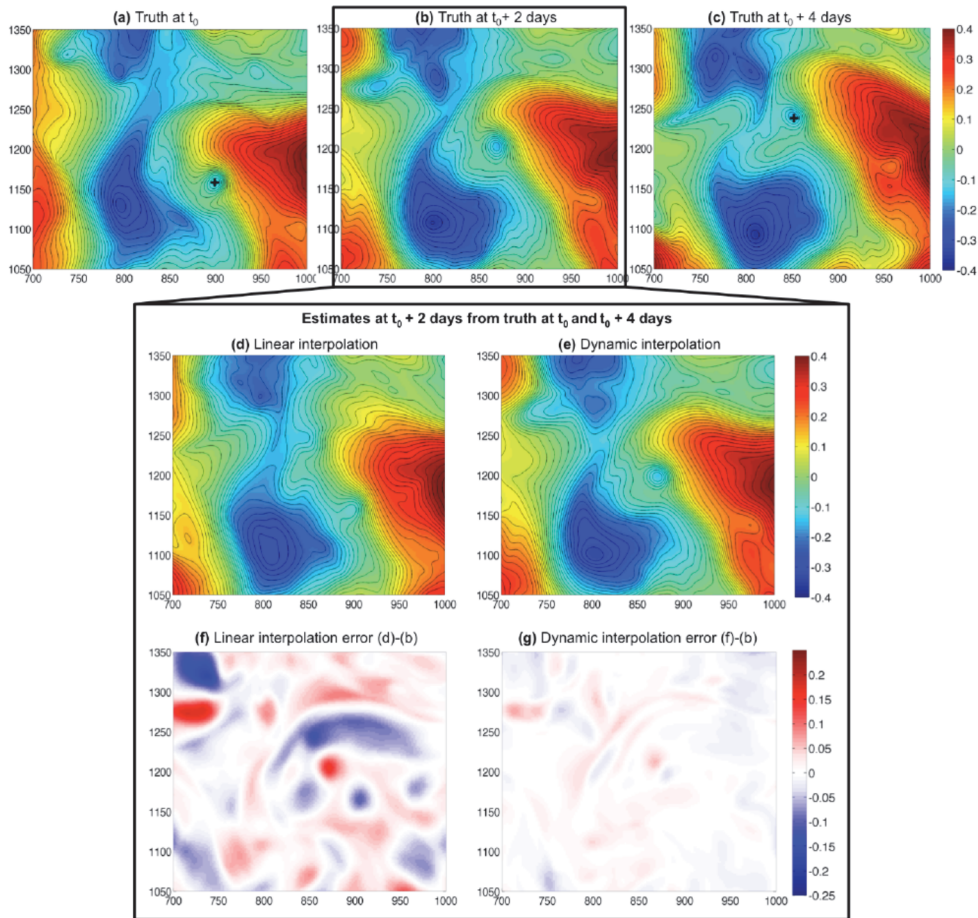


**Figure 8.20.** a,b,c: “True” SSH over a 300 km x 300 km domain at two-day intervals. d: linear SSH estimation of (b) from (a) and (c). e: dynamic SSH estimation of (b) from (a) and (c). Error fields are the difference f: between (d) and (b), and g: between (e) and (b). Units in meters. After Ubelmann et al. (2015).

In addition to the 2D reconstruction, techniques are being developed to try and diagnose the 3D dynamics in the ocean interior based on characterizing the potential vorticity (PV) field. This can allow an estimate of the 3D balanced ocean dynamics (including the vertical velocity field) using dynamical frameworks such as surface quasi-geostrophy (e.g., Lapeyre and Klein, 2006; LaCasce and Mahadevan, 2006; Wang et al., 2013; Ponte and Klein 2013; Berti and Lapeyre, 2014). The first step is to estimate surface PV at the highest possible resolution from satellite observations, either from high resolution SWOT SSH or SST as a proxy for surface density. The next step is to relate surface PV to interior PV. This can be done through a structure function that is depth-dependent (see Wang et al., 2013; Ponte and Klein, 2013) and can be estimated from climatology or the ARGO dataset if they resolve the critical layers at depth.

This surface-to-subsurface dynamical projection can be enhanced by other properties. PV is conserved along a Lagrangian trajectory and experiences a direct cascade. This means that Lagrangian techniques can allow us to recover smaller-scale structures at the surface and at depth. These techniques have proved to be very efficient. Lagrangian studies based on the temporal evolution of gridded altimetry maps have already allowed us to reconstruct ocean features with finer scales, including dynamical transport barriers aligned with the larger fronts (D’Ovidio et al., 2009, LeHahn et al., 2007) as well as finer-scale tracer fields (Despres et al., 2011; Dencausse et al., 2013). The combination of surface QG vertical projection techniques and Lagrangian advection is currently being explored (Berti and Lapeyre, 2014).

## Challenges of assimilating SWOT-simulated SSH data in operational ocean models

More sophisticated assimilation schemes are being considered to ingest SWOT-simulated SSH data into operational ocean models. Due to the large volume of SWOT data (1-2 Go/day), different direct or Lagrangian approaches are being explored. A question is how the high-resolution observations available locally along the swath will constrain the model, and what the impact on the operational analysis and forecast fields will be. The noise reduction schemes developed for 2D SSH mapping are also of use in pre-processing the SWOT data before assimilation.

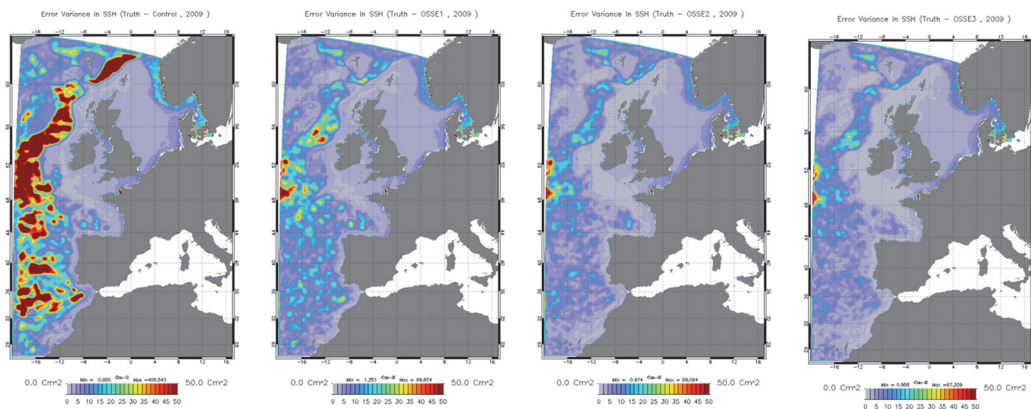


**Figure 8.21.** SSH Error variance (in  $\text{cm}^2$ ) averaged over one year – 2009 for different assimilation experiences compared to the “truth”  $1/36^\circ$  model. Error variance for a) the Free model run ( $1/12^\circ$ ) with no assimilation, b) OSSE1 assimilation with along-track Jason-2, Jason-1 and Envisat sampling, c) OSSE2 with SWOT sampling, d) OSSE3 with SWOT and along-track J2-J1-Env sampling. (Credits: M. Benkiran, Mercator-Ocean)

At Mercator-Ocean, simulated SWOT SSH data with realistic position and errors have been generated from a  $1/36^\circ$  model with tides and assimilated into a regional  $1/12^\circ$  model with tides as a testbed. At mid latitudes, the  $1/36^\circ$  “truth” data resolve scales of around 15 km, similar to SWOT, the  $1/12^\circ$  model used as the control run resolves scales of around 50 km. In these early tests, the analyzed fields have the tide and other high-frequency signals removed using a 25-h mean, to concentrate on the internal dynamics. Three cases of Observing System Simulation Experiments (OSSEs) are considered: OSSE1 with a typical sampling of three along-track altimeters based on Jason-2, Jason-1 in its geodetic phase, and Envisat tracks; OSSE2 with the SWOT 21-day sampling;

and OSSE3 with SWOT and the three altimeter sampling. Figure 8.21 shows how the error variance in the open ocean is well constrained by the SWOT sampling. Interestingly, the along-track altimeter assimilation tends to add in coherent eddy signals that evolve slowly when there are no new data assimilated. In contrast, the strong anisotropy inherent in the SWOT SSH images add a non-linear observed flow field that evolves more rapidly and more realistically during the data gaps. Due to the improved anisotropy and small-scale gradients, the relative vorticity and the sub-surface horizontal and vertical velocities are better constrained with the SWOT observations. Work is ongoing to test the assimilation with higher resolution ( $1/60^\circ$  “truth” assimilated into the  $1/36^\circ$  model) and to explore the representation and observability of the internal wave field.

Other techniques are being explored to use the complementary information from high-resolution surface tracer images (SST or ocean colour) and SWOT SSH maps to control the ocean circulation. Indeed, altimetric SSH has more energy at the larger mesoscales, whereas at smaller scales, tracer images can help control the more complex non-linear structures. Gaultier et al (2013) derived Lagrangian transport barriers from high-resolution SSH data and inverted tracer fields and assimilated these Lagrangian structures, rather than the original fields, to constrain the surface dynamics.

---

## Conclusions

Even before the SWOT launch, the promise of observing a new 2D SSH field over scales from 15-200 km is opening new research domains. Exciting questions are being explored on the role of small mesoscale and sub-mesoscale dynamics in the ocean circulation, and their impact on the energy budget, on mixing and dissipation, on the generation of larger-scale dynamics, and on the vertical exchange between the surface and deeper layers. Similar questions exist for the role of internal tides and internal waves interacting with the “balanced” ocean circulation, and modifying the eddy energy, evolution and mixing. In this chapter, we have concentrated on the dynamical fields being resolved by altimetry. Yet improving the horizontal and vertical flow at small scales will have a huge impact on the exchange of heat, carbon, and nutrients across the oceans, as well as between the surface and deeper layers, with a big impact on biogeochemical cycles and biomass evolution. Improved small-scale circulation from altimetry will be analyzed in parallel with fine-scale tracer data (SST, ocean colour) and surface parameters (surface roughness, sun-glitter, etc.), which are strongly modified across fronts and filaments, to link the deeper dynamics with the surface fronts. Finally, if SWOT data will help us validate the next generation of global, high resolution ocean models, SWOT also needs to be validated against high spatial resolution in situ data. Exploring the overlapping dynamics from small-scale internal waves and internal dynamics from existing in situ and satellite data and models will occupy a lot of our energy over the coming years.

---

## References

- Ablain M., A. Cazenave, G. Larnicol, M. Balmaseda, P. Cipollini, Y. Faugère, M. J. Fernandes, O. Henry, J. A. Johannessen, P. Knudsen, O. Andersen, J. Legeais, B. Meyssignac, N. Picot, M. Roca, S. Rudenko, M. G. Scharffenberg, D. Stammer, G. Timms, J. Benveniste, (2015). Improved sea level record over the satellite altimetry era (1993–2010) from the Climate Change Initiative project. *Ocean Science*, 11, 67-82, doi:10.5194/os-11-67-2015.
- Berti S and G Lapeyre (2014). Lagrangian reconstructions of temperature and velocities at sub-mesoscales. *Ocean Modelling*, 76, 59–71
- Birol, F., N. Fuller, F. Lyard, M. Cancet, F. Niño, C. Delebecque, S. Fleury, F. Toublanc, A. Melet, and M. Saraceno. (2017). Coastal applications from nadir altimetry: Example of the X-TRACK regional products. *Adv. Space Res*, 59(4), 936–953.
- Boy, F., J. D. Desjonquères, N. Picot, T. Moreau and M. Raynal, (2017). "CryoSat-2 SAR-Mode Over Oceans: Processing Methods, Global Assessment, and Benefits," in *IEEE Transactions on Geoscience and Remote Sensing*, 55(1), 148-158, doi: 10.1109/TGRS.2016.2601958
- Brown, G. (1977). The average impulse response of a rough surface and its applications. *IEEE transactions on antennas and propagation*, 25(1), 67-74.
- Capet A., E. Mason, V. Rossi, C. Troupin, Y. Faugere, M.-I. Pujol, A. Pascual, (2014). Implications of a Refined Description of Mesoscale Activity in the Eastern Boundary Upwelling Systems. *Geophys. Res. Lett.*, 41, doi:10.1002/2014GL061770.
- Carrere, L. and F. Lyard, (2003). Modeling the barotropic response of the global ocean to atmospheric wind and pressure forcing - comparisons with observations. *Geophys. Res. Lett.* ISSN: 0094-8276, 30, n. 6, 1275-1278.
- Chassignet, E.P. and X. Xu, (2017). Impact of horizontal resolution ( $1/12^\circ$  to  $1/50^\circ$ ) on Gulf Stream separation, penetration, and variability. *J. Phys. Oceanogr.*, 47, 1999-2021, doi:10.1175/JPO-D-17-0031.1.
- Chelton, D.B, J. C. Ries, B. J. Haines, L.-L. Fu, and P. S. Callahan, (2001). In *Satellite Altimetry and Earth Sciences: A Handbook of Techniques and Applications*; Fu, L. L.; Cazenave, A., Eds.; Academic Press: San Diego, 1–131.
- Chelton DB, Gaube P, Schlax MG, Early JJ, Samelson RM. (2011). The influence of nonlinear mesoscale eddies on near-surface oceanic chlorophyll. *Science*, 334(6054):328-32.
- Dencausse G., R. Morrow, M. Rogé and S. Fleury (2014). Lateral stirring of large-scale tracer fields by altimetry. *Ocean Dynamics*, 64, 61-78.
- Despres, A., G. Reverdin, and F. D'Ovidio, (2011). Mechanisms and spatial variability of mesoscale frontogenesis in the northwestern North Atlantic Subpolar gyre. *Ocean Modelling*, 39, 97-113, doi:10.1016/j.ocemod.2010.12.005
- Dibarboure, G., M.-I. Pujol, F. Briol, P.-Y. Le Traon, G. Larnicol, N. Picot, F. Mertz and M. Ablain, (2011). Jason-2 in DUACS: first tandem results and impact on processing and products. *Marine Geodesy*, 34, 214-241. DOI, 10.1080/01490419.2011.
- Dibarboure G, Boy F, Desjonqueres JD, Labroue S, Lasne Y, Picot N, Poisson JC, Thibaut P., (2014). Investigating short wave-length correlated errors on low-resolution mode altimetry. *J. Atmos. Ocean Technol.*, 31(6):1337–1362.
- Dong, C., J. C. McWilliams, Y. Liu, and D. Chen, (2014). Global heat and salt transports by eddy movement, *Nat Commun*, 5, <http://dx.doi.org/10.1038/ncomms4294>
- d'Ovidio, F., J. Isern-Fontanet, C. López, E. Hernández-García, and E. García-Ladona (2009), Comparison between Eulerian diagnostics and finite-size Lyapunov exponents computed from altimetry in the Algerian basin. *Deep Sea Res.*, Part I, 56(1), 15–31.
- Dufau, C., M. Orszynowicz, G. Dibarboure, R. Morrow, P.Y. Le Traon, (2016). Mesoscale Resolution Capability of altimetry: present and future. *J. Geophys. Res. Oceans*, 121, 4910–4927, doi:10.1002/2015JC010904.
- Dussurget, R., F Birol, R Morrow and P De Mey, (2011): Fine Resolution Altimetry Data for a Regional Application in the Bay of Biscay. *Marine Geodesy*, 34:3-4, 447-476.
- Escudier, P., A. Couhert, F. Mercier, A. Mallet, P. Thibaut, N. Tran, L. Amarouche, B. Picard, L. Carrère, G. Dibarboure, M. Ablain, J. Richard, N. Steunou, P. Dubois, M. H. Rio, J. Dorandeu (2017). Satellite radar altimetry: principle, geophysical correction and orbit, accuracy and precision. In: "Satellite altimetry over oceans and land surfaces". Chapter 1, Eds D. Stammer and A. Cazenave. Taylor and Francis (in press)
- Escudier, R., J. Bouffard, J., A. Pascual, P.-M. Poulain, M.-I. Pujol (2012): Improvement of coastal and mesoscale observation from space: Application to the Northwestern Mediterranean Sea. *Geophys. Res. Lett.*, 40 (10), 2148-2153
- Esteban-Fernandez, D. (2017). SWOT mission performance and Error Budget. JPL Publication D-79084.

- Fernandes, J., C. Lázaro, A. L. Nunes, and R. Scharroo (2014). Atmospheric Corrections for Altimetry Studies over Inland Water. *Remote Sens.*, 6(6), pp 4952–4997.
- Frappart, F., D. Blumstein, A. Cazenave, G. Ramillien, F. Birol, R. Morrow, F. Remy (2017). Satellite Altimetry: Principles and Applications in Earth Sciences, J. Webster (ed.), Wiley Encyclopedia of Electrical and Electronics Engineering. Copyright 2017 John Wiley & Sons, Inc. DOI: 10.1002/047134608X.W1125.pub2
- Fu, L.L. and A. Cazenave. (2001). Satellite Altimetry and Earth Sciences: A Handbook of Techniques and Applications. Academic Press: San Diego.
- Fu, LL., E Rodriguez, D Alsdorf, R. Morrow (eds). (2012). The SWOT Mission Science document. [https://swot.jpl.nasa.gov/files/swot/SWOT\\_MSD\\_1202012.pdf](https://swot.jpl.nasa.gov/files/swot/SWOT_MSD_1202012.pdf)
- Fu L.L. and C. Ubelmann (2014). On the transition from profile altimeter to swath altimeter for observing global ocean surface topography. *J. Atmos. Oceanic. Tech.*, <https://doi.org/10.1175/JTECH-D-13-00109.1>
- Garcia, E. S., D. T. Sandwell, and W. H. F. Smith. (2014). Retracking CryoSat-2, Envisat, and Jason-1 radar altimetry waveforms for improved gravity field recovery. *Geophysical Journal International*, 196(3):1402–1422.
- Garrett, C. and W Munk (1979). Internal waves in the ocean. *Ann. Review Fluid Mech.*, 11:1, 339-369
- Gaultier L., Verron J., Brankart J.-M., Titaud O. and Brasseur P., (2013). On the use of submesoscale tracer fields to estimate the surface ocean circulation. *Journal of Marine Systems*, 126, 33–42
- Gaultier, L., C. Ubelmann, and L. Fu, (2016): The Challenge of Using Future SWOT Data for Oceanic Field Reconstruction. *J. Atmos. Oceanic Technol.*, 33, 119–126, <https://doi.org/10.1175/JTECH-D-15-0160.1>
- LaCasce, J. and A. Mahadevan, (2006): Estimating subsurface horizontal and vertical velocities from sea surface temperature. *J. Marine Res.*, 64, 695–721.
- Lapeyre G, Klein P (2006). Dynamics of the upper oceanic layers in terms of surface quasigeostrophy theory. *J. Phys. Oceanogr.*, 36(2), 165-176. <http://dx.doi.org/10.1175/JPO2840.1>
- Lehahn Y., F. d'Ovidio, M. Lévy, Y. Amitai and E. Heifetz (2011). Long range transport of a quasi-isolated chlorophyll patch by an Agulhas ring. *Geophys. Res. Lett.*, 38, L16610, doi:10.1029/2011GL048588.
- Le Traon, P.Y. and G. Dibarboure, (2002). Velocity mapping capabilities of present and future altimeter missions: the role of high frequency signals. *J. Atm. Ocean Tech.*, 19, 2077-2088.
- Levy M., Iovino D., Resplandy L., Klein P., Madec G., Treguier A.-M., Masson S., Takahashi K. (2012). Large-scale impacts of sub-mesoscale dynamics on phytoplankton: Local and remote effects. *Ocean Modelling*, 43-44, 77-93. <http://dx.doi.org/10.1016/j.ocemod.2011.12.003>
- Morrow, R., L-L Fu, T. Farrar, H. Seo, P-Y Le Traon (2017). Ocean eddies and mesoscale variability. In “Satellite altimetry and its use for earth observation”, in ‘Earth Observation of Global Changes’ ed. CRC Press.
- Müller, M., B. K. Arbic, J. G. Richman, J. F. Shriver, E. L. Kunze, R. B. Scott, A. J. Wallcraft, L. Zamudio (2015), Toward an internal gravity wave spectrum in global ocean models. *Geophys. Res. Lett.*, 42, 3474–3481. doi: 10.1002/2015GL063365.
- Munk, W., (1966). Abyssal recipes. *Deep-Sea Res.*, 13 (1966), pp. 707-730
- Obligis, E., C. Desportes, L. Eymard, M. J. Fernandes, C. Lázaro, and A. Nunes (2011). In Coastal Altimetry; Springer-Verlag Berlin Heidelberg, 578, doi:10.1007/978-3-642-12796-0
- Pascual A., M.I. Pujol, G. Larnicol, P.Y. Le Traon and M.H. Rio (2005). Mesoscale Mapping Capabilities of Multisatellite Altimeter Missions: First Results with Real Data in the Mediterranean Sea. *J. Mar. Systems*, 65, 190–211, doi:10.1016/j.jmarsys.2004.12.004.
- Pascual, A., Faugere, Y., G. Larnicol, P.Y. Le Traon, (2006). Improved description of the ocean mesoscale variability by combining four satellite altimeters. *Geophys. Res. Letters*, 33 (2): Art. No. L02611.
- Peral, E. E. Rodriguez, D. Esteban-Fernandez (2015). Impact of surface waves of SWOT’s projected ocean accuracy *Remote Sens.* 7(11), 14509-14529; doi:10.3390/rs71114509
- Ponte A, Klein P (2013). Reconstruction of the upper ocean 3D dynamics from high-resolution sea surface height. *Ocean Dynamics*, 63(7), 777-791. <http://dx.doi.org/10.1007/s10236-013-0611-7>
- Ponte A, Klein P (2015) Incoherent signature of internal tides on sea level in idealized numerical simulations. *Geophys. Res. Lett.*, 42: 1520–1526. doi: 10.1002/2014GL062583.
- Pujol, M. I. Larnicol, G, (2005). Mediterranean Sea eddy kinetic energy variability from 11 years of altimetric data, *J. Mar. Systems*, 58, 121-142.
- Pujol, M.-I., Y. Faugère, G. Taburet, S. Dupuy, C Pelloquin, M. Ablain, N. Picot (2016). DUACS DT2014: the new multi-mission altimeter dataset reprocessed over 20 years. *Ocean Sci. Discuss.*, doi:10.5194/os-2015-110.
- Pujol, M.-I., P. Schaeffer, Y. Faugère, M. Raynal, G. Dibarboure, N. Picot (2018). Gauging the improvement of recent mean sea surface models: a new approach for identifying and quantifying their errors. *J. Geophys. Res.*, submitted.

- Qiu B, T Nakano, S Chen, P Klein (2017). Submesoscale transition from geostrophic flows to internal waves in the northwestern Pacific upper ocean. *Nat Comm.*, 8:14055. doi:10.1038/ncomms14055
- Quartly, G. D., M. A. Srokosz, and A. C. McMillan, (2001): Analyzing altimeter artifacts: Statistical properties of ocean waveforms. *J. Atmos. Oceanic Technol.*, 18, 2074–2091, doi:10.1175/1520-0426(2001)018<2074:AAASPO>2.0.CO;2
- Raney, R.K. (1998) "The delay/Doppler radar altimeter" IEEE Trans. Geosci. Remote Sens vol. 36 no. 5 pp. 1578-1588.
- Ray R.D. and Zaron E.D., (2016). M2 internal tides and their observed wavenumber spectra from satellite altimetry. *J. Phys. Oceanogr.*, 46:1, 3-22, doi:10.1175/JPO-D-15-0065.1.
- Richman, J. G., B. K. Arbic, J. F. Shriver, E. J. Metzger, and A. J. Wallcraft, (2012): Inferring dynamics from the wavenumber spectra of an eddying global ocean model with embedded tides. *J. Geophys. Res.*, 117, C12012, doi:10.1029/2012JC008364.
- Robinson, I.S., (2004). Measuring the oceans from space. Praxis-Springer-Verlag, 669pp.
- Rocha, C.B., T. K. Chereskin, S. T. Gille, and D. Menemenlis (2016) Mesoscale to Submesoscale Wavenumber Spectra in Drake Passage. *J. Phys. Oceanogr.*, 46:2, 601-620. doi:10.1175/JPO-D-15-0087.1
- Rodriguez, E, D Esteban Fernandez, E Peral, C W Chen, J-W De Bleser, B Williams (2017). Wide-swath altimetry: A review. In: "Satellite altimetry over oceans and land surfaces", Book Chapter 2. Eds D. Stammer & A. Cazenave, Taylor and Francis.
- Rogé, M., Morrow, R., Ubelmann, C., and Dibarboure, G. (2017). Using a Dynamical Advection to Reconstruct a Part of the SSH Evolution in the Context of SWOT, Application to the Mediterranean Sea. *Ocean Dynamics*, 1-20, doi:10.1007/s10236-017-1073-0.
- Sasaki H., Klein P., Qiu B., Sasai Y. (2014). Impact of oceanic-scale interactions on the seasonal modulation of ocean dynamics by the atmosphere. *Nature Comm*, 5, 1-8.
- Shriver, J. F., B. K. Arbic, J. G. Richman, R. D. Ray, E. J. Metzger, A. J. Wallcraft, and P. G. Timko (2012), An evaluation of the barotropic and internal tides in a high-resolution global ocean circulation model. *J. Geophys. Res.*, 117, C10024, doi:10.1029/2012JC008170.
- Stammer, D., R.D. Ray, O.B. Andersen, B.K. Arbic, W. Bosch, L. Carrere, Y. Cheng, D.S. Chinn, B.D. Dushaw, G.D. Egbert, S.Y. Erofeeva, H.S. Fok, J.A.M. Green, S. Griffiths, M.A. King, V. Lapin, F.G. Lemoine, S.B. Luthcke, F. Lyard, J. Morison, M. Müller, L. Padman, J.G. Richman, J.F. Shriver, C.K. Shum, E. Taguchi, and Y. Yi, (2014): Accuracy assessment of global barotropic ocean tide models. *Reviews of Geophysics*, 52, 243-282, doi:10.1002/2014RG000450.
- Ubelmann, C., P. Klein, L.-L. Fu (2015) Dynamical interpolation of sea surface height and potential applications for future high-resolution altimetry mapping. *J. Atmos. Ocean. Tech.*, 32, 177-184, doi: 10.1175/JTECH-D-14-00152.1
- Ubelmann, C., B. Cornuelle, and L. Fu (2016) Dynamic Mapping of Along-Track Ocean Altimetry: Method and Performance from Observing System Simulation Experiments. *J. Atmos. and Oceanic Tech.*, 33:8, 1691-1699. doi:10.1175/JTECH-D-15-0163.1
- Verron, J., Sengenes, P., Lambin, J., Noubel, J., Steunou, N., Guillot, A., Picot, N., Coutin-Faye, S., Sharma, R., Gairola, R. M., Raghava Murthy, D. V. A., Richman, J. G., Griffin, D., Pascual, A., Rémy, F., and Gupta, P.K., (2015): The SARAL/AltiKa altimetry satellite mission. *Mar. Geod.*, 38, 2–21, doi:10.1080/01490419.2014.1000471.
- Vignudelli S, Kostianoy AG, Cipollini P, Benveniste J. (eds.) (2011). Coastal Altimetry, Springer-Verlag Berlin Heidelberg, 578, doi:10.1007/978-3-642-12796-0
- Wang, J., G.R. Flierl, J.H. LaCasce, J.L. McClean and A. Mahadevan, (2013). Reconstructing the ocean's interior from surface data. *J. Phys Oceanogr.*, 43, 1611-26, doi:10.1175/JPO-D-12-0204.1
- Wunsch C (1997). The vertical partition of oceanic horizontal kinetic energy. *J. Phys. Oceanogr.*, 27(8):1770–1794. doi:10.1175/1520-0485(1997)027<1770:TVPOOH>2.0.CO;2
- Xu, Y., and L-L. Fu, (2012): The effects of altimeter instrument noise on the estimation of the wavenumber spectrum of sea surface height, *J. Phys. Oceanogr.*, 42, 2229-2233. doi:10.1175/JPO-D-12-0106.1



